JGR Solid Earth

RESEARCH ARTICLE
10.1029/2020JB021133

Physics-Based Earthquake Simulations in Slow-Moving Faults: A Case Study From the Eastern Betic Shear Zone (SE Iberian Peninsula)

Paula Herrero-Barbero[1], José A. Álvarez-Gómez[1], Charles Williams[2], Pilar Villamor[2], Juan M. Insua-Arévalo[1], Jorge Alonso-Henar[1], and José J. Martínez-Díaz[1,3]

[1]Department of Geodynamics, Stratigraphy and Paleontology, Universidad Complutense de Madrid, Madrid, Spain, [2]GNS Science, Lower Hutt, New Zealand, [3]Geosciences Institute (UCM-CSIC), Madrid, Spain

Key Points:

- The RSQSim earthquake simulator reproduces a realistic 100 kyr synthetic catalog of $M_W > 4.5$ events based on a slow fault system
- Large earthquakes, even $M_W \geq 7.0$, and complex multifault ruptures are possible despite their nonoccurrence in historical times
- The synthetic seismic cycles have variable interseismic time periods, so the different time frames should be considered in hazard studies

Supporting Information:

Supporting Information may be found in the online version of this article.

Correspondence to:

P. Herrero-Barbero,
pherrerob@ucm.es

Citation:

Herrero-Barbero, P., Álvarez-Gómez, J. A., Williams, C., Villamor, P., Insua-Arévalo, J. M., Alonso-Henar, J., & Martínez-Díaz, J. J. (2021). Physics-based earthquake simulations in slow-moving faults: A case study from the Eastern Betic Shear Zone (SE Iberian Peninsula). *Journal of Geophysical Research: Solid Earth*, *126*, e2020JB021133. https://doi.org/10.1029/2020JB021133

Received 7 OCT 2020
Accepted 10 APR 2021

The copyright line for this article was changed on 19 AUG 2021 after original online publication.

Abstract In regions with slow-moving faults, the incompleteness of earthquake and fault data complicates the study of seismic hazard. The instrumental and historical seismic catalogs cover a short period compared with the long-time interval between major events. Paleoseismic evidence allows us to increase the time frame of actual observations, but data is still scarce and imprecise. Physics-based earthquake simulations overcome the limitations of actual earthquake catalogs and generate long-term synthetic seismicity. The RSQSim earthquake simulator used in our study reproduces the earthquake physical processes based on a 3D fault model that contains the kinematics, the long-term slip rates and the rate-and-state friction properties of the main seismogenic sources of a region. The application of earthquake simulations to the Eastern Betic Shear Zone, a slow fault system at southeastern Spain, allows the compilation of 100 kyr-synthetic catalogs of $M_W > 4.0$ events. Multisection earthquakes and complete ruptures of some faults in this region, preferentially on strike-slip dominant ruptures, are possible according to our simulations. The largest $M_W > 6.5$ events are likely as a result of jumping ruptures between the Carboneras and the Palomares faults, with recurrence times of < 20,000 years; and less frequently between the Alhama de Murcia and the Los Tollos faults. A great variability of interevent times is observed between successive synthetic seismic cycles, in addition to the occurrence of complex co-ruptures between faults. Consequently, the occurrence of larger earthquakes, even $M_W \geq 7.0$, cannot be ruled out, contrasting with the low to moderate magnitudes recorded in the instrumental and historical earthquake catalog.

1. Introduction

Earthquake hazard forecasting often has to deal with the scarcity of seismicity data, the complexity of fault segmentation, the uncertainties derived from the characterization of seismogenic sources, the dynamics of earthquake rupture and the recurrence model used. Instrumental earthquake recordings are available only since about 1900 and they are not reliable until several decades later. There are a few regions with representative historical data of large earthquakes for more than 2000 years in Italy (Boschi, 2000), Japan (Ishibashi, 2004), and China (Liu et al., 2011) that allow acquisition of reliable major earthquake magnitudes and recurrence statistics. In regions with low to moderate seismicity, such as some zones of the western Mediterranean or intracontinental areas, earthquake hazard estimation is especially challenging (see e.g., Estay et al., 2016; Gamage & Venkatesan, 2019; Perea & Atakan, 2007). Most of the large, and consequently damaging earthquakes, have recurrence times on the order of hundreds or thousands of years. Since historical catalogs are often scarce and imprecise, the paleoseismic record provides valuable data about rare but devastating major events and long-term recurrence times, but these data usually have large uncertainties (McCalpin, 2009). Often, the slow fault systems, besides generating low seismicity in terms of frequency, show little geomorphological expression. This makes it difficult to define the segmentation of fault traces and the parameters relating to their 3D geometry and their kinematics. Fault system geometry also plays an important role in the stress interactions that control the earthquake ruptures and therefore magnitude and recurrence statistics (e.g., Dieterich & Richards-Dinger, 2010; Steacy & McCloskey, 1999; Stirling et al., 1996).

Table 1
$M_W \geq 6.0$ Events in the Eastern Betic Shear Zone Since 1400 AD With the Epicentral Coordinates, Intensity, and Magnitude

Year	Epicentral area	Lat (°)	Long (°)	I_{EMS}	M_W	$\pm\sigma$	Evidence of association with a fault section (references)
1482	Orihuela (Alicante)	38.08	−0.92	VIII	6.0	0.8	Onshore BSF (spatial correlation - García-Mayordomo, 2005)
1487	Almeria	36.83	−2.47	VIII	6.0	0.8	Epicentral location is uncertain
1518	Vera (Almeria)	37.23	−1.87	VIII-IX	6.2	0.8	Southern PF (spatial correlation - García-Mayordomo et al., 2012)
1522	Alhama de Almeria	36.97	−2.67	VIII-IX	6.5	0.3	Northern CF (Reicherter & Hübscher, 2007)
1658	Almeria	36.83	−2.47	VIII	6.0	0.8	Epicentral location is uncertain
1673	Orihuela (Alicante)	38.08	−0.92	VIII	6.0	0.6	Onshore BSF (spatial correlation - García-Mayordomo, 2005)
1674	Lorca (Murcia)	37.68	−1.70	VIII	6.0	0.8	AMF - Goñar-Lorca section (Martínez-Díaz et al., 2018)
1804	Dalias (Almeria)	36.77	−2.83	VIII-IX	6.4	0.2	Loma del Viento fault (Campo de Dalías) (Murphy, 2019)
1829	Torrevieja (Alicante)	38.08	−0.68	IX-X	6.6	0.2	Onshore BSF, San Miguel de las Salinas F. or Torrevieja F. (spatial correlation - García-Mayordomo et al., 2006)
1910	Adra (Almeria)	36.67	−3.37	VIII	6.1	0.4	Adra Fault (Gràcia et al., 2012); minor NW-SE and N-S faults (Stich et al., 2003; Rodríguez-Escudero et al., 2014)

Note. Data from the earthquake catalog homogenized in moment magnitude MW (IGN-UPM, 2013). Fault correlations are based on published studies (see references). BSF: Bajo Segura fault; PF: Palomares fault; CF: Carboneras fault; AMF: Alhama de Murcia fault.

The Eastern Betic Shear Zone (EBSZ; De Larouzière et al., 1988) is a good example of a region with slow-moving faults and moderate seismicity where the scarcity of data and its uncertainties complicate the study of seismic cycles. Some of the largest historical earthquakes occurring in the Betic Cordillera (SE Spain) are related to this active fault system (Stich et al., 2020). Since the fifteenth century, 10 earthquakes with intensity $I_{EMS} >$ VIII have been recorded (Table 1), implying possible $M_W \geq 6.0$ magnitudes (IGN-UPM, 2013). Regarding the instrumental seismicity, the most damaging event occurring in Spain in the last decade was the 2011 Lorca earthquake (M_W 5.1). This earthquake, despite its moderate magnitude, caused 9 fatalities, around 300 injured people and severe damage to the city of Lorca (Figure 1), highlighting the possible devastating consequences of a major event in a densely populated area such as SE Spain. This recent event has been related to the activity of the EBSZ and provides valuable insight on rupture behavior (López-Comino et al., 2012; Martínez-Díaz, Bejar-Pizarro, et al., 2012). Paleoseismological research has provided evidence of post-Pleistocene paleoearthquakes in some faults of the EBSZ (Table 2) which are inferred to be larger than M_W6. In general terms, the time elapsed between these paleoevents with surface ruptures on a specific fault section ranges from circa one thousand to tens of thousands years. Note that the historical catalog covers a short period compared with this long time interval between major paleoevents.

The absence of large earthquakes in the instrumental catalog and the lack of information about the possible rupture behavior hinder the estimation of location, timing, and intensity of ground motions in the seismic hazard assessments in the EBSZ. Co-rupture of several fault sections and even of different faults, as it has been observed in some worldwide earthquakes (e.g., 2016 Kaikoura, 2010 Haiti, and 2010 El Mayor-Cucapah earthquakes; see Clark et al., 2017; Hayes et al., 2010; Oskin et al., 2012, respectively), is an issue that raises important questions in the EBSZ. Some paleoseismic evidence of large surface displacements in the zone support a combined rupture of different segments of the same fault in a single event (Ortuño et al., 2012). For these joined ruptures to occur, not only stress transfer and kinematic compatibility are required, but also the sections and faults involved should be close to failure, so that they can generate a seismic event effectively. Therefore it would be essential to observe the seismicity of a low strain region for several complete seismic cycles in order to appropriately estimate the likelihood of possible scenarios.

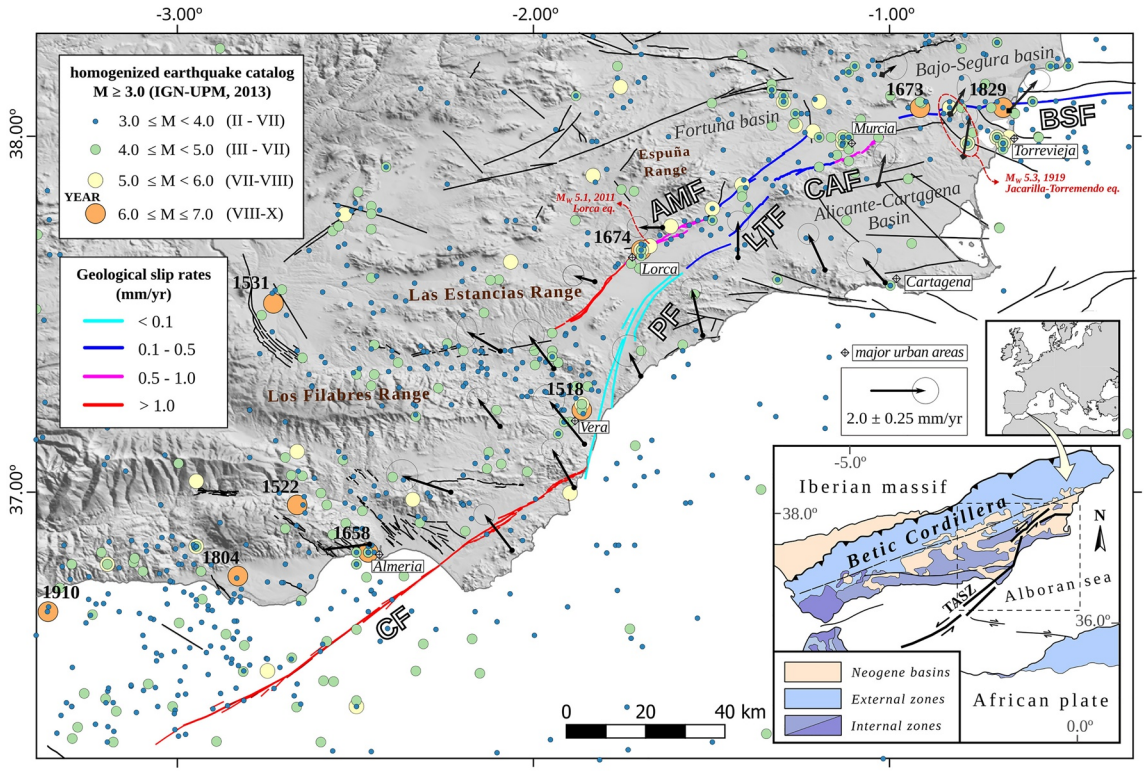

Figure 1. Seismotectonic setting of the Eastern Betic Shear Zone (EBSZ). Seismicity data from the homogenized earthquake catalog used for recent maps of seismic hazard of Spain (IGN- UPM, 2013). The arrows represent geodetic velocity trends from GNSS networks (Borque et al., 2019; Echeverria, Khazaradze, Asensio, Gárate, et al., 2013) with Eurasia-fixed reference frame. Fault traces in black are taken from the Quaternary Active Fault Database of Iberia, QAFI v.3 (García-Mayordomo, Insua-Arévalo, et al., 2012). The faults of the EBSZ analyzed in this study are represented with colors according to the mean geological slip rate estimated (see references in Table 3). These faults are: Carboneras fault (CF), Alhama de Murcia fault (AMF), Palomares fault (PF), Los Tollos fault (LTF), Carrascoy fault (CAF), and Bajo-Segura fault (BSF). TASZ: Trans-Alboran Shear Zone.

Synthetic seismicity models can overcome the limitations of real earthquake catalogs and reproduce long-term realistic catalogs from a set of seismic sources. Among these models, the application of physics-based earthquake simulators (initial concept introduced by Rundle (1988)), have been extended satisfactorily in the last decades for seismic hazard studies in Greece, New Zealand and California, among others (see e.g., Console, Carluccio, et al., 2015; Robinson et al., 2011; Shaw et al., 2018). The earthquake simulation codes use the physics of stress interactions and frictional properties to reproduce the processes that control the earthquake nucleation and rupture propagation in order to output a synthetic catalog lasting a fixed time duration.

In this study, we use the RSQSim earthquake simulator (Richards-Dinger & Dieterich, 2012) to simulate synthetic seismicity in the EBSZ. The RSQSim simulator is based on a boundary element formulation that integrates rate- and state-dependent friction (Dieterich, 1978) to calculate the sliding resistance between interacting fault surfaces. We generate a 3D model of the main seismogenic sources of the EBSZ that contains data related to each fault, such as long-term slip rates and rakes. This is the first attempt to incorporate the physical processes that control earthquake occurrence, frictional properties, and stress interactions into a hazard study for this fault system. The application of the earthquake simulator on this fault model results in synthetic catalogs that span 100 kyr and contain thousands of $M_W > 4.5$ events. These catalogs are long enough for statistical analysis of events and the comparison with some observations of the seismicity data in the EBSZ. We analyze long-term recurrence between large earthquakes and the characteristics of the rupture. The analysis of interactions between faults of the system provides us information about maximum magnitudes, interevent time intervals and rupture behavior in the EBSZ.

Table 2
Evidence of Paleoearthquakes in the EBSZ, Obtained Through Different Methodologies: Paleoseismic Trenching, Tectonic Geomorphology, Archaeoseismology

Fault section	No of paleoevents	Date (kyr)	Slip per event (error) in meters	Comments
AMF-1	≥ 4	<125.0	1.13 (0.86–1.40) V 0.56 (0.35–0.76) S	Observed in trenches from different sites (Ortuño et al., 2012; Martínez-Díaz, Masana, & Ortuño, 2012; Martínez-Díaz et al., 2018).
AMF-2	[a]5 – 8 [b]3 – 7	<26.9 <31.0	0.45 (0.43–0.45) V 0.64 (0.16–0.95) D	[a]From Masana et al. (2004) in El Saltador-Colmenar paleoseismic sites and the analysis of García-Mayordomo (2005). [b]From Canora et al. (2016) in La Salud fan.
AMF-3	1	<3.6	0.18 S; 0.07 (0.05–0.08) V	Archaeoseismological analysis in La Tira del Lienzo Bronze Age site (Ferrater et al., 2015).
CF-2	[c] ≥ 4 [d] ≥ 3	<133.0 <41.5	1.5 (0–3) S	[c]Events since the Mid Pleistocene observed in Los Trances site (Masana et al., 2018). [d]Paleoearthquakes and max. slip per event observed in El Hacho site (Moreno, 2011).
PF-2	2	<200.0	0.95 (0.64–1.24) N	Analysis of faulted fan surfaces and paleosols by Roquero et al. (2019).
LTF	≥ 2	2.74–2.14	0.46 (0.39–0.54) N	Data analysis from paleoseismic trenches (Insua-Arévalo et al., 2015).
CAF-1	9 – 11	<30.2	1.19 (1.05–1.23) N	Obtained from paleoseismic trenches (Martín-Banda et al., 2016).

[a]*Note*. The slip per event values and the number of paleoearthquakes represent measurements taken at a certain paleoseismic site. See fault sections names in Table 3. AMF: Alhama de Murcia fault; CF: Carboneras fault; PF: Palomares fault; LTF: Los Tollos fault; CAF: Carrascoy fault. N is net slip; V is vertical slip; S is strike slip; D is dip-slip.

2. Seismogenic Sources in the Eastern Betic Shear Zone

The EBSZ (Figure 1) is located in the Eastern Betic Cordillera (SE Iberian Peninsula) and constitutes the Betic onshore prolongation of the Trans-Alboran Shear Zone (De Larouzière et al., 1988). It is an active deformation zone mainly formed by strike-slip faults, some of which have a reverse slip component to a greater or lesser extent. The main seismogenic faults of the EBSZ are, from south to north (Figure 1): Carboneras fault (CF), Palomares fault (PF), Alhama de Murcia fault (AMF), Los Tollos fault (LTF), Carrascoy fault (CAF) and Bajo Segura fault (BSF). For references about the research on aforementioned faults, see Tables 2 and 3, Supporting Information (Table S1) and the Quaternary Active Fault Database of Iberia, QAFI v.3 (García-Mayordomo, Insua-Arévalo, et al., 2012).

A neotectonic shortening phase started at the end of the Neogene as a result of Eurasia and Africa convergence (Sanz de Galdeano, 1990; Herrero-Barbero et al., 2020, and references therein). Present-day convergence rate is about 4–6 mm/yr in a NW-SE direction based on geodetic and seismological data (see e.g., Koulali et al., 2011; Nocquet, 2012; Serpelloni et al., 2007) and the EBSZ seems to be accommodating up to 31% of the total shortening (Masana et al., 2004). Regional GNSS data (Figure 1) suggest a geodetic slip-rate of 1.5 ± 0.3 mm/yr in the middle part of the EBSZ, including AMF and PF zones (Echeverria, Khazaradze, Asensio, Gárate, et al., 2013), whereas in the NE end of the EBSZ, GPS networks record 0.6 ± 0.2 mm/yr of shortening at BSF zone (Borque et al., 2019).

The Eastern Betic Cordillera is characterized by low to moderate instrumental seismicity with typical magnitudes of $M_W < 5.5$ (García-Mayordomo, Gaspar-Escribano, & Benito, 2007; Rodríguez-Escudero et al., 2014). In the last decade, the biggest earthquake recorded was the 2011 M_W 5.1 Lorca earthquake (López-Comino et al., 2012), which had an intensity I_{EMS} VII and reached a maximum peak acceleration of 0.36 g, resulting in heavy casualties −9 people died–and significant economic losses. This earthquake has been interpreted as the result of the AMF activity (Figure 1) by Martínez-Díaz, Bejar-Pizarro, et al. (2012). The instrumental catalog shows other seismic series of moderate intensity in the EBSZ over the last 50 years: Lorca 1977 (M_W 4.2); Adra 1993–1994 (M_W 5.0); Bullas 2002 (M_W 5.0); and La Paca 2005 (M_W 4.8). These earthquakes have been associated with small faults located across the shear zone (Rodríguez-Escudero et al., 2014). Even

Table 3
Input Parameters Assigned to the fault Sections Modeled for the Eastern Betic Shear Zone (EBSZ)

Fault name	Fault section name	ID	Rake	Deviation	Slip rate	Deviation	References
Alhama de Murcia Fault (AMF)	Góñar–Lorca	AMF-1	20	0–40	1.10	0.50–1.70	R from slickenlines measured by Martínez-Díaz (1998). SR based on trenches (Ferrater et al., 2017; Ortuño et al., 2012)
	Lorca–Totana	AMF-2	39	19–59	0.90	0.80–1.00	R from 2011 Lorca eq.(Martínez-Díaz, Bejar-Pizarro, et al., 2012) and structural analysis by Alonso-Henar et al. (2020). SR from trenching and morphotectonic analysis (Ferrater et al., 2016; Ferrater et al., 2017)
	Totana–Alhama de Murcia	AMF-3	42	25–58	0.20	0.07–0.32	Data inferred from AMF-4
	Alhama de Murcia–Alcantarilla	AMF-4	42	25–58	0.20	0.07–0.32	SR and R from cross-section restorations (Herrero-Barbero et al., 2020). Min.SR from Silva et al. (2003).
Carboneras Fault (CF)	Southern Carboneras (offshore)	CF-1	10	0–20	1.20	1.10–1.30	Data from deflected submarine channels in CF-1 (Moreno, 2011) and onshore fluvial channels in CF-2 (Moreno et al., 2015). Max. SR based on GPS data of Echeverria et al. (2015)
	Northern Carboneras (offshore-onshore)	CF-2	10	0–20	1.20	1.10–1.30	
Palomares Fault (PF)	Southern Palomares–Arteal Faults	PF-1	−5 (0)	(-25) - 15	0.04	0.01–0.08	Data measured by Booth-Rea et al. (2004), comparing fluvial deposits and paleochannels in PF-1. R in PF-2 is consistent with the moment tensor of a recent M_W3.6 event (IGN, 2019)
	Northern Palomares (S[a] Almenara)	PF-2	15	0–35	0.04	0.01–0.08	
	Northern Palomares–Hinojar Faults	PF-3	15	0–35	0.10	0.04–0.16	R is inferred from PF-2 and SR is based on comparison between PF-3 and LTF-1
Los Tollos Fault (LTF)	Los Tollos Fault	LTF-1	15	0–35	0.16	0.06–0.25	R and SR obtained through trenching by Insua-Arévalo et al. (2015).

Table 3
Continued

Fault name	Fault section name	ID	Rake	Deviation	Slip rate	Deviation	References
Carrascoy Fault (CAF)	SW Carrascoy–Algezares–Casas Nuevas	CAF-1	90	75–90	0.37	0.29–0.45	R and SR estimated from trenches by Martín-Banda et al. (2016). R is referred to the younger reverse branch (see Table S1).
	NE Carrascoy Fault	CAF-2	15	5–25	0.85	0.50–1.20	Data from structural analysis (Martín-Banda, 2020; Sanz de Galdeano et al., 1998; Silva, 1994).
Bajo Segura Fault (BSF)	Hurchillo	BSF-1	90	70–110	0.40	0.29–0.51(0.6)	SR estimations from Alfaro et al. (2012) using stratigraphic markers and assuming pure reverse. Note that GPS data from Borque et al. (2019) show 0.6 ± 0.2 mm/yr of shortening for the entire BSF zone
	Benejúzar	BSF-2	90	70–110	0.27	0.20–0.34	
	Guardamar	BSF-3	90	70–110	0.20	0.15–0.25	
	Bajo Segura Offshore	BSF-4	90	70–110	0.20	0.15–0.25	For R, see seismic profiles from Alfaro et al. (2012) and Perea et al. (2012). SR is inferred from BSF-3

Note. See Supporting Information (Table S1) for more detailed data about the criteria followed to assign the mean, maximum, and minimum values according to references. R: rake (°); SR: slip rate (mm/yr).
Rake is defined using the Aki and Richards (1980) convention (right-hand rule). If uncertainties cannot be quantified, a default value of ± 20° is used.

though no significantly destructive earthquakes have happened in the Eastern Betics for the last century (except for 2011 Lorca earthquake), the historical catalog contains very damaging events with intensities I_{EMS} > VII since the fifteenth century. The 1829 Torrevieja earthquake (I_{EMS} IX-X), the 1522 Alhama de Almería earthquake (I_{EMS} VIII-IX) and the 1674 Lorca earthquake (I_{EMS} VIII), have seismic sources associated with sections of the EBSZ (see references in Table 1). It has been estimated that these historical damaging earthquakes could reach magnitudes $M_W \geq 6.0$ (Table 1; IGN-UPM, 2013). In pre-historic times, evidence of surface ruptures has allowed the identification and dating of $M_W \geq 6.0$ paleoearthquakes (Table 2) in several fault sections.

The most recent models of the EBSZ in seismic hazard studies have combined the delimitation of seismogenic zones with the dimensions and rates of fault sources (e.g., García-Mayordomo, 2005; García-Mayordomo, Gaspar-Escribano, & Benito, 2007; IGN-UPM, 2013; Villamor, 2002), incorporating, for example, the generation of synthetic frequency-magnitude data from slip rates (Gómez-Novell et al., 2020) and the distribution of the seismic potential between zones and faults using the events of the seismic catalog for certain periods of completeness (Rivas-Medina et al., 2018). So far, no attempts have been made to also incorporate the physical processes that control earthquake occurrence in fault systems, the frictional properties and the stress interactions, as we present in this study to evaluate the seismic potential in the EBSZ.

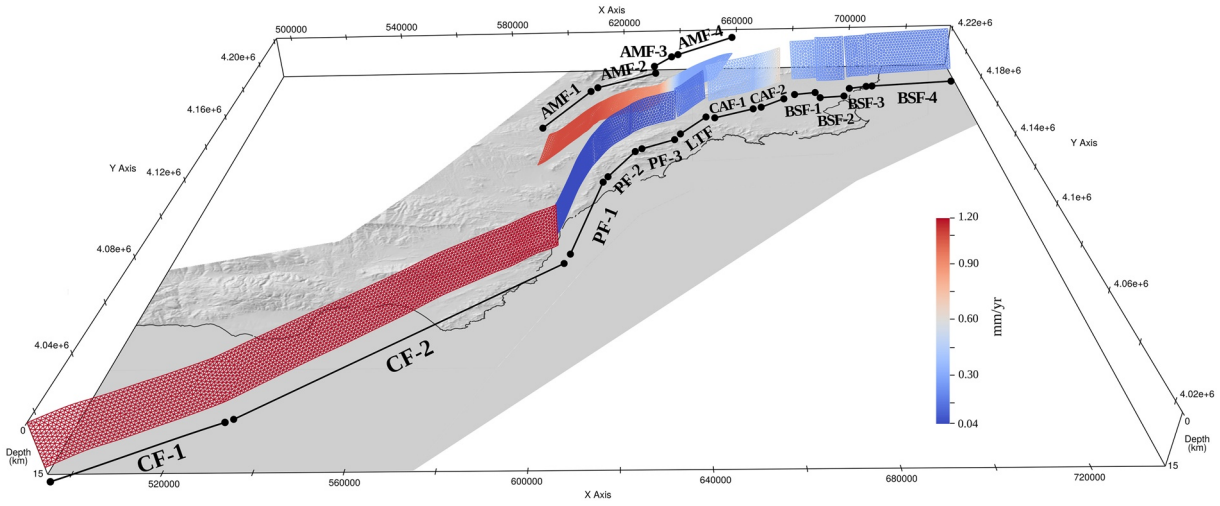

Figure 2. Three-dimensional model of the main seismogenic faults of the EBSZ and the slip rates assigned.

3. Methodology

To simulate the seismicity of a region by means of synthetic earthquake models, we need three main components: a geometrical model of seismogenic sources with long-term slip rates, a model of fault rock frictional properties, and a physics-based simulation code, in our case, the RSQSim earthquake simulator (Richards-Dinger & Dieterich, 2012).

3.1. 3D Geometrical and Strain Model

We have produced a three-dimensional model of the EBSZ (Figure 2). The model reproduces the geometrical characteristics of the faults both along strike and down-dip. The segmentation of faults in the EBSZ is generally based on geometry of the fault zone, seismicity, and relief of the hanging wall (see e.g., Alfaro et al., 2012; Martí et al., 2020; Martínez-Díaz, Masana, & Ortuño, 2012; Moreno et al., 2016). In Table 3, we show the segmentation model and the slip-rate values based on the review of recent studies that estimate multiple activity parameters (see references in the Table). We simplified the fault sections with several strands to a single trace representative of its geometry to avoid abrupt boundaries in the model. We considered seismogenic crustal depths between 8 and 12 km based on seismotectonic studies at Southeastern Spain (García-Mayordomo, 2005). See Table S1 of Supporting Information for detailed data on fault geometry (dip angle, fault length), criteria followed, methods, ages considered in the estimations and complete references.

Fault slip rates (Table 3) have been estimated at local sites along the fault system taking into account multiple methodologies (trenches, geophysics and marker restorations, among others) and the results are extrapolated to the entire fault section. Most of faults in the EBSZ are left-lateral reverse-oblique faults [mean rake angle ≤ 45° based on the Aki and Richards (1980) convention], except for the reverse BSF (Alfaro et al., 2012; Taboada et al., 1993) and one of the branches of the CAF (Martín-Banda et al., 2016). Rake angles (Table 3) are moderately constrained from field data and they can be highly variable for a single fault (Kearse et al., 2019). The rake value, together with the slip rate, is essential in our fault model because each fault element will be initially allowed to slip only in its assigned rake direction (Richards-Dinger & Dieterich, 2012). For this reason, we have assessed the reliability of the input parameters of Table 3 using similar methodologies to García-Mayordomo, Martín-Banda, et al. (2017) and Litchfield et al. (2013) for rating the quality of the data. Our qualitative classification of data is shown in Tables S2 and S3 of the Supporting Information.

RSQSim considers a system of faults as multiple boundary elements embedded in a homogeneous half-space. We developed meshes with triangular elements at a resolution of 1 km^2, using the software *Trelis*. The

Table 4
Rate-and-State Friction Parameters, Initial Normal (σ_0) and Shear (τ_0) Stress Conditions and Gutenberg-Richter B-value Obtained From Frequency Distribution of Synthetic Seismicity

Catalog	a	b	$a-b$	σ_0 (MPa)	τ_0 (MPa)	b-value (M_c 4.6)
cat-3	0.010	0.015	−0.005	120	60	1.50 ± 0.01
cat-14	0.001	0.008	−0.007	100	60	0.99 ± 0.00
cat-20	0.010	0.015	−0.005	20[a]	60	1.65 ± 0.01
cat-21	0.001	0.006	−0.005	20[a]	60	1.25 ± 0.01
cat-27	0.001	0.008	−0.007	20[a]	60	1.13 ± 0.01
cat-28	0.001	0.010	−0.009	20[a]	60	1.05 ± 0.00
cat-29	0.001	0.010	−0.009	140	75	1.08 ± 0.00

Note. We used the software ZMAP 7 (Wiemer, 2001) for the analysis of seismicity. An optimal magnitude of completeness M_C 4.6 is calculated for moderate-sized events based on the complete set of catalogs, which have variable number of events and different minimum magnitudes, two of them larger than M_W 4.

[a]These values represent a gradient of 20 MPa/km.

use of triangular elements allows us to build more realistic curved fault surfaces (Gilchrist, 2015), while the use of 1 km^2 as the minimum cell size improves the seismic catalog, helping to reduce the stress concentrations at the model elements for more realistic ruptures (Dieterich, 1995; Gilchrist, 2015; Richards-Dinger & Dieterich, 2012). Our fault model of the EBSZ (Figure 2) described above contains 11,764 elements.

3.2. Frictional Properties

RSQSim incorporates rate- and state-dependent friction equations (Dieterich, 1978) to simulate earthquakes. In Appendix A, the RSQSim simulator formulation is described. The rate-and-state friction parameters control the nucleation and propagation of earthquakes (e.g., Dieterich, 1979; Scholz, 1998). In the EBSZ, some experimental studies explore the frictional properties of fault rocks from the region (Niemeijer & Vissers, 2014; Rodríguez-Escudero, 2017). We assigned the global frictional parameters of the fault model based on the best-fit results of these studies. Multiple simulations were carried out in order to tune the frictional parameters to match observed earthquake magnitude-rupture area scaling relations (Leonard, 2010; Wells & Coppersmith, 1994), a procedure followed by numerous modeling studies before (e.g., Console, Vannoli, & Carluccio, 2018; Shaw et al., 2018; Wilson et al., 2018). It is an iterative process and the aim is to generate a frequency distribution of moderate-sized events similar to the behavior of instrumental seismicity in the Eastern Betic region, with a Gutenberg-Richter b-value close to 1.0 ± 0.1 (García-Mayordomo, 2005; IGN-UPM, 2013; Villamor, 2002).

3.3. RSQSim simulations

In the simulations, input parameters are assigned for each fault element in the model. The tectonic stressing rate over the fault surfaces is applied by means of the back-slip method (Savage, 1983) using the mean geologic fault slip rates presented in Table 3. The cycle of stress accumulation and seismic slip at each element is simplified in terms of three states: locked, nucleation, and sliding. Among other features, Equation A1 (see Appendix A) shows that in RSQSim the stress drop during an event is logarithmically dependent on slip velocity and proportional to the product of the normal stress and the difference of the state and rate coefficients (a–b). Stress interactions between elements (Equation A3 and A4) are based on 3D elasto-static dislocation solutions (Gimbutas et al., 2012; Okada, 1992).

RSQSim makes a quasi-dynamic approximation to rupture nucleation and propagation. During seismic rupture, every fault element that slips transfers stress to the rest of the model, but there are no dynamic interactions (i.e., waveforms) and other subsequent dynamic effects (e.g., ground motions and off-fault deformations). In the RSQSim simulations, earthquakes nucleate spontaneously and the nucleation location for each individual event is not specified *a priori*, hence each simulated rupture has a set of initial stress conditions. It is a computational approach which makes it significantly faster than fully dynamic models. Despite all stresses in RSQSim are based purely on elastostatic calculations, the code introduces some enhancements to achieve a better validation of the quasi-dynamic part of the earthquake phenomenon (see "Approximations to Elastodynamics" of Richards-Dinger and Dieterich (2012)). In our model of the EBSZ, we deal with the dynamic limitations through the application of a dynamic stress overshoot factor (10%), the reduction of rate-coefficient a in the rate- and state-dependent friction law, and the variation of initial stresses (see input parameters of the simulation in Table S4), which seems to emulate successfully the space-time evolution of the rupture governed by fully-dynamic models (Gilchrist, 2015; Richards-Dinger and Dieterich, 2012).

Simulations have been therefore run varying the rate-and-state friction parameters and also the initial stress conditions (Table 4). Friction coefficients are varied in each simulation as a single parameter with no spatial variation. RSQSim simulations begin with homogeneous initial shear stress, but during simulations, the

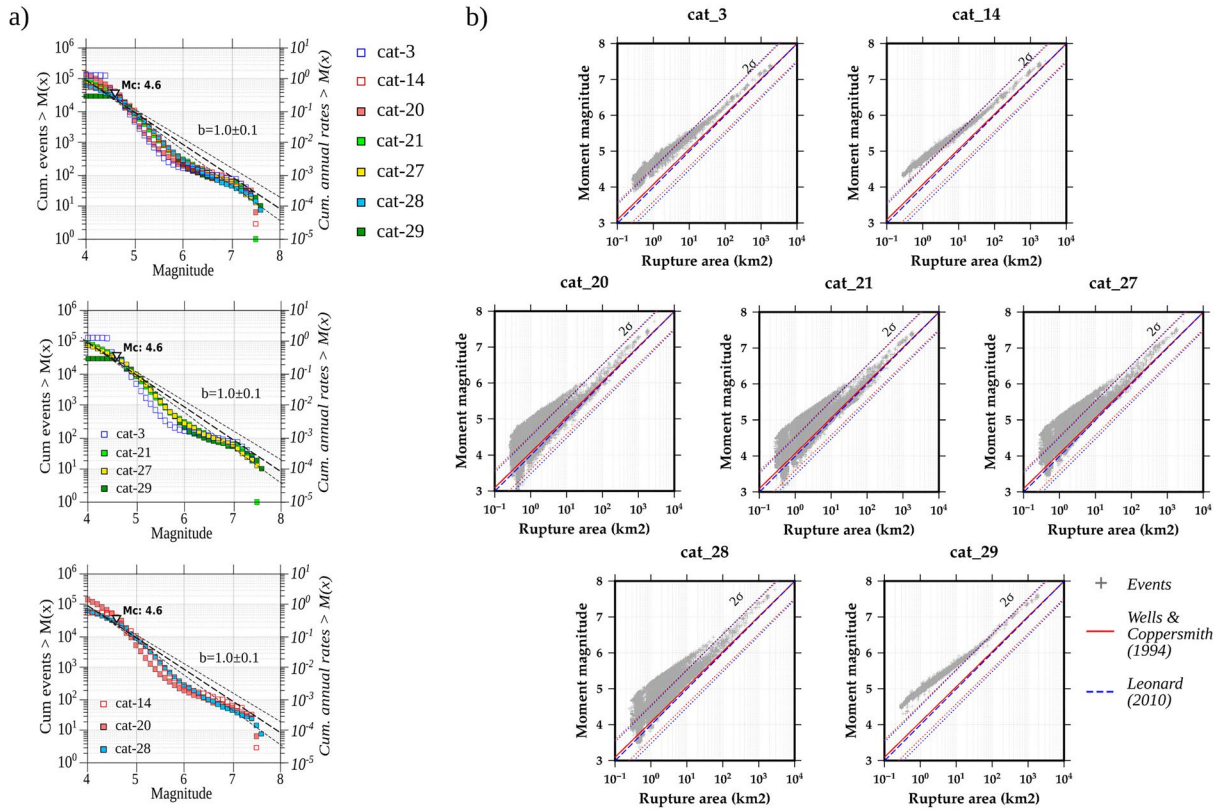

Figure 3. Statistical comparison between the synthetic catalogs obtained using the RSQSim earthquake simulator code. (a) Cumulative earthquakes > $M(x)$ and frequency-magnitude distributions for the earthquake catalogs. We estimate an optimal magnitude of completeness M_C 4.6 for moderate-sized events considering all the catalogs. (b) Magnitude-rupture area distribution of the synthetic seismicity against the scaling relations (Leonard, 2010; Wells & Coppersmith, 1994). Dotted lines represent two standard deviations derived from the uncertainties of the regressions used.

shear stress evolves through fault system interactions over many seismic cycles but never reaches the value assigned for the first event, which is 60 MPa in our simulations. We tried a variable initial normal stress with a gradient of 20 MPa/km because we observed during the iterations that this model allowed us to homogenize the slope of the magnitude distribution and simulate more realistic ruptures (Richards-Dinger & Dieterich, 2012). This improves the comparison between the synthetic catalog and the instrumental catalog of the EBSZ, which contains mostly small events. Nevertheless, the nonuniform normal stress is clearly evident in the first simulated event but has almost disappeared in subsequent events, thus it does not affect the modeling of slip in the rupture propagation (Gilchrist, 2015; Lapusta & Liu, 2009), although it could sometimes condition re-nucleation in adjacent faults (Oglesby, 2008, see section 5.3 of the Discussion). The first 2000 years in the catalogs are discarded in order to avoid the irregularities in the first ruptures before the stress state has evolved. The comparison of the seismicity from the simulations with the empirical relationships has been made after applying a process of seismicity declustering on the catalogs (Reasenberg, 1985) using the software *ZMAP* (Wiemer, 2001), which is standard practice in seismic hazard analyses. Later discussion of a specific catalog has been conducted without applying the declustering method, except when the analysis required it.

See the data sets available in a public data repository (Herrero-Barbero et al., 2021) for more details about the 3D fault model, input data for RSQSim simulations (including test simulations) and output data: earthquake catalogs, slip data, and statistical analysis.

Table 5
Comparison Between synthetic Catalogs That Best fit the Frequency-Magnitude and Magnitude-Rupture Area Scaling Relations (Figure 3). f Represents the Ratio Between Mean RI of Paleoseimic Sites and Mean RI of the Synthetic Catalogs, Referring to Equation 1

		cat-20		cat-21		cat-27		cat-28	
Site	[a]RI_{site} (*kyr*)	RI_{cat} (*yr*)	f	RI_{cat} (*yr*)	f	RI_{cat} (*yr*)	f	RI_{cat} (*yr*)	f
AMF-2	4.8 ± 1.9	4,021.9	1.19	4,115.8	1.16	3,940.1	1.21	4,561.9	1.05
CF-2	23.5 ± 9.7	1,505.3	15.64	832.8	28.27	999.7	23.55	1,016.9	23.15
LTF	4.5 ± 2.3	9,705.1	0.47	9,063.3	0.50	10,195.5	0.45	9,803.9	0.46
CAF-1	3.3 ± 0.7	7,935.8	0.42	6,378.9	0.52	7,953.1	0.41	12,166.0	0.27
BSF-2	9.6 ± 0.2	14,790.4	0.65	9,410.4	1.02	11,665.7	0.83	10,167.8	0.95
MAD			*0.41*		*0.29*		*0.38*		*0.34*

Note. MAD: Mean absolute deviation (excluding the CF-2 values).
[a]See Table 2 and Text S1 of the supporting information for data and criteria used to calculate RI_{site}.

4. Results

The multicycle simulations result in synthetic catalogs lasting 100,000 years that range from 28,000 events in some cases to almost 300,000 in others. The magnitudes cover a range of $3.0 < M_W < 7.6$, although two of the catalogs have minimum magnitudes larger than M_W 4. The input parameters influence the extent of the catalogs, but we acknowledge that, due to the size of the mesh and the quasi-dynamic limitations of the simulation code, the smallest earthquake ruptures may not be entirely realistic. Figure 3 shows the frequency-magnitude distribution (FMD) and magnitude-rupture area relations obtained from the simulated catalogs. The FMD (Figure 3a) shows that magnitudes $M_W < 5.5$ and $M_W > 6.5$ from the modeled catalogs fit quite well with the range of b-value = 1. 0 ± 0.1 observed in the study area. For magnitudes M_W 5.5–6.5, however, a change in slope from ~1.0 to 1.2 is observed. This discrepancy for moderate magnitudes is also observed in other studies that create synthetic catalogs using earthquake simulators (e.g., Christophersen et al., 2017; Sachs et al., 2012) and is a result of the lack of small fault elements in the model. The use of an element size of 1 km^2 and the frictional parameters assigned in our model allow us to reach a minimum earthquake magnitude of M_W 3.4, but the optimal magnitude of completeness of the catalogs is calculated to range from M_C 4.0 to 4.6. The synthetic catalog should have a greater number of earthquakes of $M_W < 5$ compared to the number of $M_W > 5$ so that the projection of its FMD could approximate the slope of the actual seismicity. Theoretically, the fault model could be created with patches smaller than 1 km^2, however this would require a significant increase in the computation time and does not serve the objectives of this study. For subsequent discussions of this study, we will take minimum magnitudes of M_W 4.5 or 5.0.

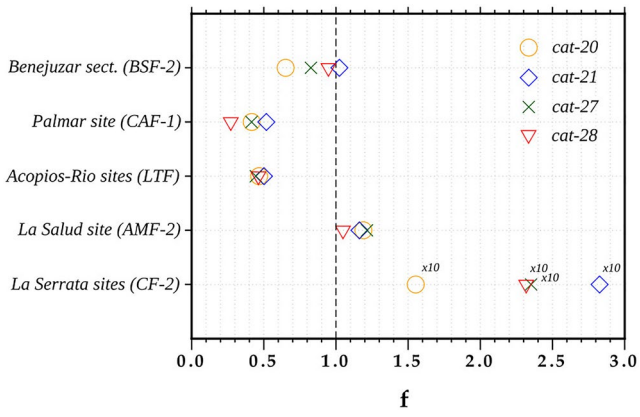

Figure 4. Comparison between the recurrence intervals (RI) for $M_W > 6$ simulated earthquakes with those obtained in the paleoseismic sites of the EBSZ (see Text S1 for further details about the data from the paleoseismic sites). The factor *f* is calculated for each synthetic catalog.

There are some evident differences between the synthetic catalogs with respect to how they fit the magnitude-rupture area relation (Figure 3b). Overall, the best-fit results match the catalogs with rate-and-state friction parameter $a = 0.001$ (Table 4), except for catalogs 29 and 14, which have great discrepancies (Figure 3b). The catalogs with $a = 0.01$ (cat-20 and cat-3; Table 4) demonstrate good correlation but differ on the earthquake scaling relations for the small magnitudes (Figure 3b). In catalogs 27 and 28, which show better correlation with the magnitude-rupture area scaling relations (Figure 3b), there is again a slight discrepancy regarding the optimal trend for the largest magnitudes ($M_W > 7$).

To identify the synthetic catalogs that better fit the known seismicity characteristics of the EBSZ, the recurrence intervals (RI) for $M_W > 6$ simulated earthquakes have been compared with those obtained for the faults using paleoseismological methods (Table 2). We selected 5 representative paleoseismic sites where recurrence times have been estimated

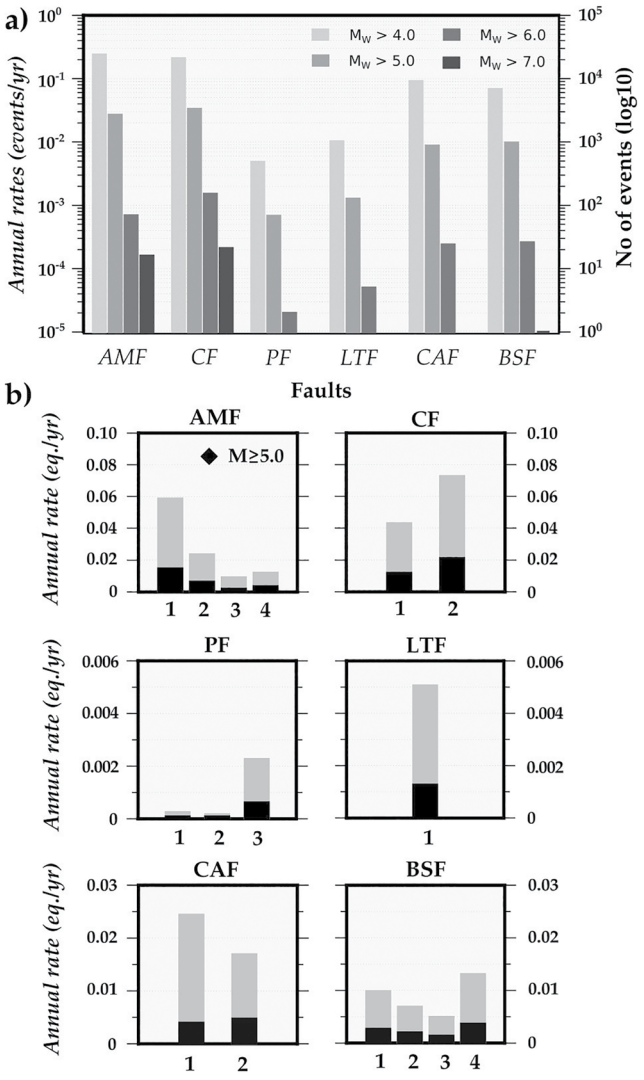

Figure 5. Catalog statistics from the reference simulation. (a) Number of events and annual rates (in logarithmic scale) nucleated on each fault of the system for several ranges of magnitudes. (b) Annual rates of $M_W \geq 4.5$ earthquakes for each fault section of the model. $M_W \geq 5.0$ events are emphasized in black.

through observations of surface paleoruptures in trenches (Table 5). For estimating RI, we considered the time span between the first and the last observed or simulated events in relation to the number of events. The ratio between mean RI of paleoseimic sites and mean RI of the synthetic catalogs results in a factor:

$$f = \frac{RI_{site}}{RI_{catalog}} \quad (1)$$

that allows comparison of the modeled catalogs (Table 5 and Figure 4) that best fit the observed empirical relations previously analyzed (Figure 3). This is a simplification of the procedure applied in the earthquake rupture forecast for California (UCERF; Field et al., 2008), where there are much more paleoseismic data that allow for more complex statistical comparisons. The synthetic catalogs that best fit the magnitude-area observations are: 20, 21, 27, and 28 (Figure 3b). First, we observe that the results agree better with the paleoseismic data obtained for the La Salud site in AMF-2 and for the Benejuzar section in BSF (Figure 4). The results for the CF are, however, overestimated in relation to the observations in trenches. According to the mean deviation around the factor *f*, the catalogs 21 and 28 are those that best correlate with data obtained in paleoseismic sites of the EBSZ (Table 5), together with the good results of the magnitude-rupture area scaling observations (Figure 3b).

We have selected catalog 28 for the rest of the analyses of this study. Besides the good correlation between the recurrence data, the magnitude-rupture area plot (Figure 3b) roughly fits the scaling relationships (Leonard, 2010; Wells & Coppersmith, 1994), with a better equivalence for magnitudes $4.0 < M_W < 6.5$. The magnitude-frequency plot (Figure 3a) shows that the slope has the best solution for a b-value of 1.05 (Table 4). Therefore, the combination of parameters that resulted in better agreement with the criteria of seismicity distribution are: rate-and-state friction parameters $a = 0.001$ and $b = 0.010$, a steady-state coefficient of friction $\mu_0 = 0.6$, an initial shear stress of 60 MPa and a variable initial normal stress of 20 MPa/km with depth. See Table S4 of Supporting Information for the rest of input parameters used in the simulation analyzed (e.g., critical slip distance D_C of Equation A1 and Lamé elastic moduli).

The multicycle simulation assumed as a reference case based on the geometrical, strain, and frictional properties of the faults at the EBSZ results in a synthetic catalog of 77,245 events (after the first 2000 years are discarded, see above). The synthetic catalog spans a range of magnitudes between $3.4 \leq M_W \leq 7.6$, although we have taken a range of $4.5 \leq M_W \leq 7.6$ for the following interpretations. Figure 5 shows some catalog statistics from the reference simulation. For a 100 kyr period, 75% of fault ruptures in the EBSZ are associated with the AMF and the CF (Figure 5a). The largest number of earthquakes are nucleated in the southern sections of the AMF (Figure 5b), as expected because of their greater estimated slip rates (AMF-1 and AMF-2; see Table 3). AMF-4 has more seismicity than AMF-3 despite having the same slip rate (Figure 5b); in this case the determining factor could be the greater length of the AMF-4 section. In the CF, most of the hypocenters are located in the northern section, probably also because of the greater length of this section that favors a wider rupture area. The PF and the LTF show a similar magnitude distribution (Figure 5a) but the latter, which is modeled as a unique section (Figure 2), is the source of a greater number of events. CAF and BSF, located at the northeast of the fault zone, show very similar seismicity statistics (Figure 5a). The southwestern section of the CAF generates more synthetic events despite its slower slip rate. The fault section of the BSF with the highest seismicity

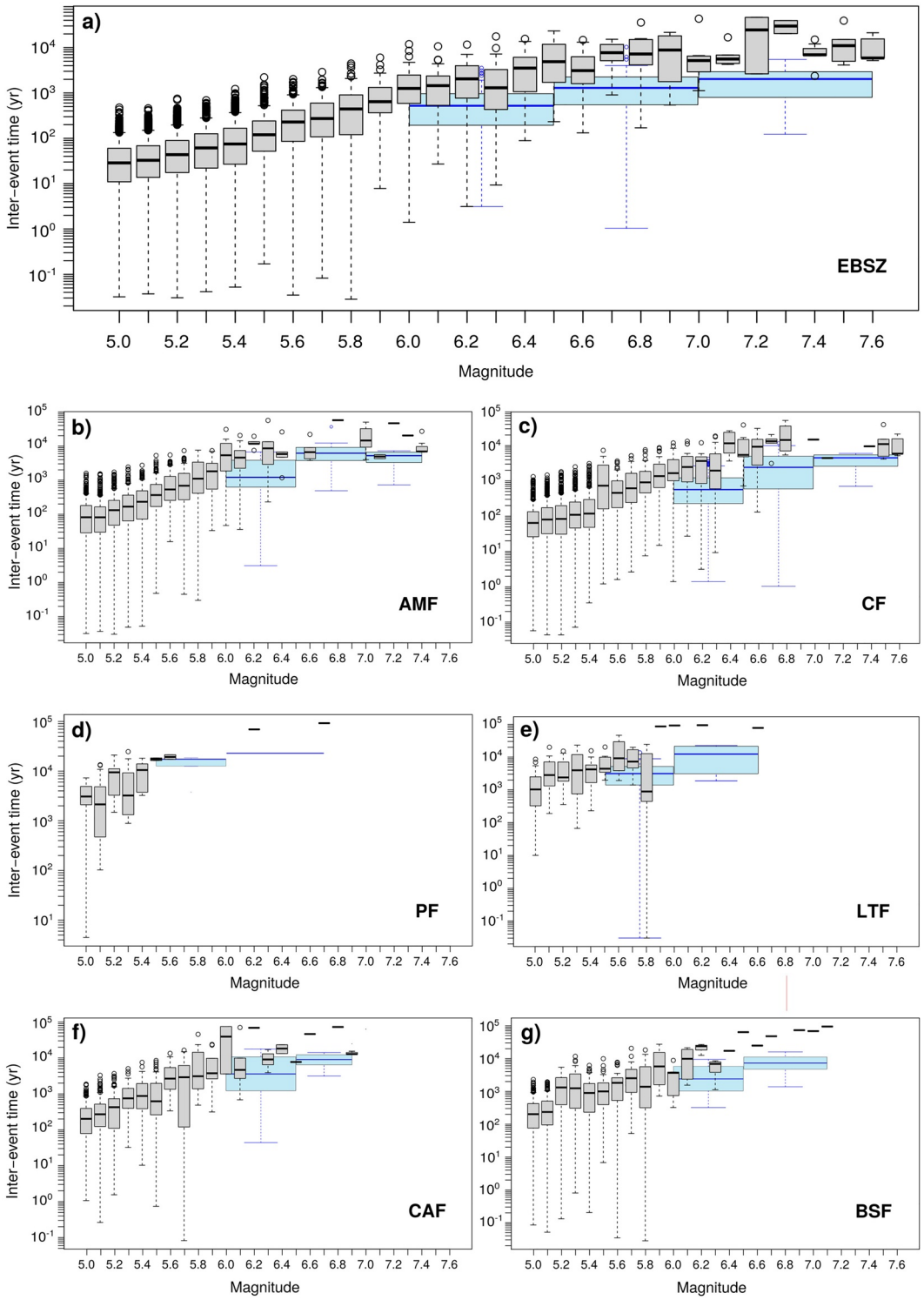

Figure 6. Interevent time distribution according to moderate-large moment magnitudes simulated on (a) the complete fault system and, (b) to (g), on each fault. The gray box lies between the upper and lower quartiles of the data, the black line inside the box indicate the median value, the dashed lines represent maximum and minimum values, and the isolated circles are the outliers. The blue boxes show interevent times for less frequent $M_W \geq 6$ earthquakes ($M_W \geq 5.5$ for PF and LTF) considering a larger magnitude bin. Events with an intermediate time less than 10 days have been discarded to avoid a clustering effect.

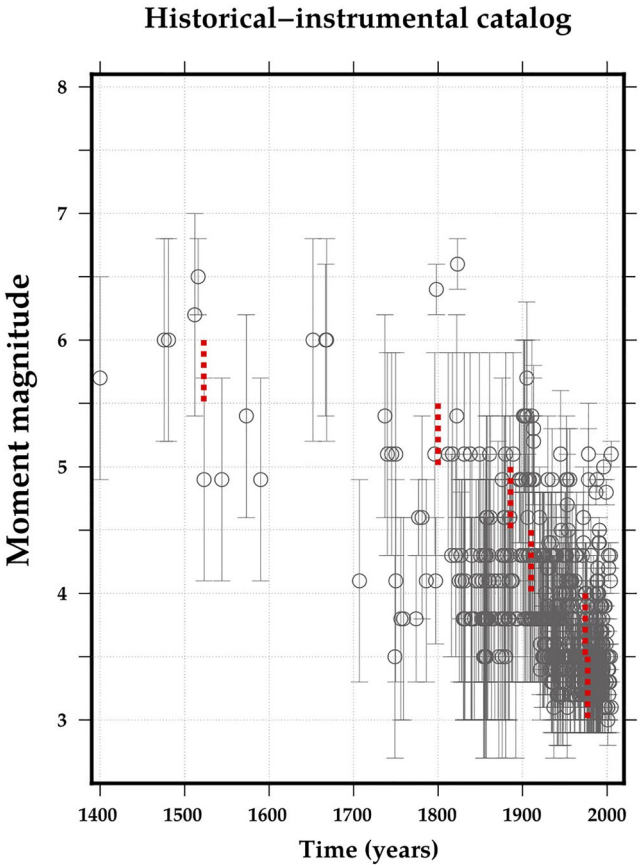

Figure 7. Historical-instrumental $M_W > 3$ seismicity in the region of study, from the refined and homogenized earthquake catalog of moment magnitudes by IGN-UPM (2013).The red dashed lines represent the years of completeness of the historical catalog for each interval of magnitudes shown in Table 6.

would be the offshore branch (BSF-4), which is mapped with a greater length (Figure 1).

Earthquakes with magnitudes greater than M_W 5.0 represent only 10.5% of the simulated seismicity (black bars in Figure 5b). The simulation suggests that all the faults of the system can nucleate $M_W \geq 6.0$ events, even the PF with two M_W 6.2 and 6.7 events for the 100 kyr time frame. $M_W > 7$ synthetic earthquakes are nucleated only on the AMF and the CF, except for a single event recorded on the BSF. The maximum magnitude recorded for the AMF is M_W 7.4, reached in several events on AMF-1 or AMF-2. The maximum magnitude of the entire synthetic catalog, M_W 7.6, occurs in the northern section of the CF. The maximum magnitudes simulated on the LTF, the CAF, and the BSF are M_W 6.6, M_W 6.9, and M_W 7.1, respectively.

When we calculate the average RI to compare the simulated catalogs, we assume a periodic occurrence of earthquakes along the studied time span as a way to approximate the recurrence of large events in a particular fault. If we analyze in detail the time between events nucleated by the simulations (Figure 6), we observe a logical progressive increase with magnitude of the most probable interevent time values. According to the simulated seismicity for the entire fault system (Figure 6a), the most probable interevent times for moderate magnitudes M_W 5.5–6.0 range between 70 and 2000 years; and for magnitudes M_W 6.0–6.5 the time intervals rise from 800 years to approximately 7000 years. From magnitude M_W ~6.5, the process seems to become more stochastic, possibly influenced by the different fault section areas interacting with each other. Due to this uncertainty, the largest magnitudes have been grouped into wider intervals (blue boxes in the plot) allowing a more conservative interpretation of the interevent times obtained. The distribution of interevent times and magnitudes varies with each fault. In general, we see similarities in the behavior of recurrence and of the maximum magnitudes between pairs of faults: AMF with CF (Figures 6b and 6c), PF with LTF (Figures 6d and 6e), and CAF with BSF (Figures 6f and 6g).

5. Discussion

The application of a physics-based earthquake simulator to the EBSZ, the main active fault system of the Eastern Betic Cordillera, SE Spain, has allowed the compilation of a 100 kyr synthetic seismic catalog for $M \geq 4.5$ events. This catalog contains 75,977 earthquakes whose magnitude distribution tries to emulate the observed regional seismicity, but without the limitations of real catalogs concerning the completeness and short time duration. In this section, we compare in detail the resulting synthetic catalog with the real instrumental and historical catalogs of the region. We analyze the similarities found in the paleoseismological data from each fault, emphasizing some issues of the catalog that demand more detailed discussion.

5.1. Analysis of Magnitudes and Interevent times

As mentioned before, the observed seismicity data related to the Eastern Betics is quite limited and incomplete. The instrumental catalog dates back to 1923 A.D. (Gaspar- Escribano et al., 2015) and historical macroseismic intensities are mostly dated after the fifteenth century (Martınez-Solares & Mezcua, 2002). The project to update the maps of seismic hazard in Spain (IGN-UPM, 2013) compiles a refined and homogenized earthquake catalog of moment magnitudes (Table 1) from macroseismic and instrumental data. From this earthquake catalog, we have selected $M_W > 3$ seismicity geographically correlated with the faults of our model (see Figure 7 and the complete list in Dataset S1 of Supporting Information), assuming a buffer of ~30 km wide to both sides of the mapped trace. Note that the standard deviations of the greatest magnitude estimations are very large (Table 1). According to this earthquake catalog of the study region,

the time period available for real seismicity data is barely 600 years (Figure 7). However, the completeness analysis of the seismic catalog for the SE of Spain (IGN-UPM, 2013), confirms that the year of completeness for small $3 \leq M_W \leq 3.9$ earthquakes is quite recent, 1975; and for $4 \leq M_W \leq 4.9$ earthquakes the reference year is 1883. Therefore, the actual catalog for the study region is not easily comparable with the synthetic 100 kyr catalog obtained due to its incompleteness and the uncertain location of many epicenters. We will analyze the occurrence of certain magnitude intervals and interevent times of the simulated seismicity in relation to similar earthquakes recorded in the historical catalog.

The synthetic catalog shows that the seismogenic sources with the greatest number of nucleated events (Figure 5a) are the AMF and the CF, located at the southwestern half of the fault system (Figure 1). This fact is due to assigned slip rates > 1 mm/yr in some of their sections. It is possible that the predominant strike-slip kinematics (low angles of rake) favored long ruptures, linking fault sections and hence large rupture areas. The southern section of the AMF (AMF-1) has been correlated by Martínez-Díaz et al. (2018) with the 1674 Lorca earthquake (Table 1) with an estimated magnitude of M_W 6.0 ± 0.8. Despite the high uncertainty in the estimation of magnitude, the synthetic catalog provides evidence of numerous modeled events of similar size (Figure 5b). Interevent time intervals (Figure 6b) range from 100 years (median value) for magnitudes close to M_W 5, to 5,000 years for magnitudes around M_W 6. For higher magnitudes, the sample of synthetic events decreases, increasing the resulting interevent time variability, with a maximum of 50,000 years. From a more conservative approach, if we group the magnitudes into wider intervals (M_W 6.0–6.5, M_W 6.5–7.0, $M_W \geq 7.0$; blue boxes), we observe that for $M_W > 6.5$ earthquakes, the most likely interevent times vary between 4000 and 9000 years in the AMF.

The CF seems to be the source of a historical earthquake that occurred in 1522, with an estimated magnitude of M_W 6.5 ± 0.3 (Alhama de Almeria earthquake; Table 1). According to Reicherter and Hübscher (2007), this historic earthquake might be associated with the northern section (CF-2), where our synthetic models simulate a large nucleation of events with similar magnitudes (Figure 5b). The interevent time intervals in this case are estimated to be around 500 and 2000 years for magnitudes similar to the 1522 earthquake, if we consider the values of the statistics with larger (~0.5) sample interval (blue boxes in Figure 6c). The time intervals decrease to values between 30 and 300 years for 50% of the earthquakes $5 \leq M_W < 5.5$ in the catalog.

The northeastern part of the EBSZ (Figure 1) has also exhibited intense seismic activity during historical and instrumental periods (Giner et al., 2003). Several of the largest earthquakes with I_{EMS} > VII (Table 1) have occurred here, namely the 1482 and 1673 Orihuela earthquakes, and the 1829 Torrevieja earthquake. The latter is the event with the largest intensity recorded in the historical catalog of the region (Martınez-Solares & Mezcua, 2002) and an estimated magnitude around M_W 6.6 ± 0.2 (IGN-UPM, 2013). The seismogenic sources located northeast of our EBSZ model are CAF and BSF (Figure 2). Both faults generate synthetic events with maximum magnitudes M_W 6.9–7.1, slightly higher than the estimated magnitude for the Torrevieja earthquake. The simulated seismicity in the CAF and the BSF suggests a higher probability of interevent times of more than 100 years and less than 3,000 years for $M_W < 6$ magnitudes (Figures 6f and 6g). These interseismic periods of a few hundreds of years are on the order of that observed in the real historical record of the zone (Table 2).

The variability of interevent time intervals along successive seismic cycles emphasizes one of the main problems of the historical-instrumental catalog: the influence of the time frame. Figure 8 shows the synthetic seismicity obtained in time intervals of 600 years, similar to the time window of real seismicity available at EBSZ, but with a maximum completeness of the 100 kyr catalog for magnitudes greater than M_W 4.5. In this example, we observe that after the occurrence of the largest earthquake, an expected increase of smaller events is generated (Figure 8a), most of them of moderate-sized ($M_W \geq 5.5$). According to this, up to 4 events with magnitude greater than M_W 6.0 may occur in barely 100 years. This cluster of large events, or "earthquake storm" (Nur & Cline, 2000), occurs when a great event in one fault section produces a stress load on adjacent sections causing successive earthquakes to be triggered in the following days, months or years. After this cluster, in the consecutive interval of 600 years (Figure 8b), a period of quiescence without big earthquakes is revealed, once the system has released all the accumulated stress after the sequence of major events. The moderate background seismicity observed during these long periods is also seen, for example, after the New Madrid ~ M_W8 intraplate earthquakes in the 1800s, where no events of similar magnitude have occurred since then but a low ongoing seismicity has remained so far (Page & Hough, 2014).

Table 6
Annual Occurrence Rates Estimated for Moderate-Small Synthetic Earthquakes and for Regional Historical Seismicity

		Annual occurrence rate (events/yr)	
Magnitude M_W	Year of completeness (IGN-UPM, 2013)	Historical catalog	Synthetic catalog
4.5–4.9	1883	0.24 ± 0.15	0.23
5.0–5.4	1800	0.08 ± 0.03	0.07
5.5–5.9	1520	0.01 ± 0.01	0.01
6.0–6.4	1048	0.005 ± 0.004	0.002

Note. We take the historical events from the years of completeness calculated by IGN-UPM (2013) for intervals of magnitudes.

Additionally, Figure 8c shows another time frame of 600 years far from the previous ones, in which two pairs of events close to M_W6 occur. In this case, no larger earthquake is generated throughout the same time interval as the previous examples. Therefore it is evident that there is a strong influence of the time scale when analyzing even a single seismic cycle (Figures 8a and 8b). According to the long-term simulations performed, we cannot rule out the occurrence of sequences of larger size than those recorded in the historical catalog, especially in regions with slow-moving seismogenic faults and long interseismic periods.

Smaller earthquakes ($M_W < 6.0$) occur more frequently at Eastern Betics, and some of them have been quite damaging despite their moderate magnitude, thus we should pay due attention to them. Faults of the EBSZ included in our model are the most likely seismogenic sources for some of those events, for example: 2011 Lorca earthquake (M_W 5.1) and 1919 Jacarilla-Torremendo earthquakes (M_W 5.3), associated with the fault zones of the AMF (Martínez-Díaz, Bejar-Pizarro, et al., 2012) and the BSF (Batlló et al., 2015), respectively (Figure 1). Some minor earthquakes may also have seismic sources associated with smaller faults not included in our model (Rodríguez-Escudero et al., 2014, see subsection 5.4). We have approached the estimation of annual occurrence rates for moderate-small earthquakes recorded in both catalogs (Table 6). For the rates of the regional historical seismicity, we have taken only the events from the years of completeness calculated by IGN-UPM (2013) for each interval of magnitude. We observe a relatively good correlation of annual occurrence rates for the entire fault system (Table 6) despite the great interevent time variability observed in synthetic seismicity. The simulations generate an annual occurrence rate of 0.23 events/yr for magnitudes M_W 4.5–4.9. For magnitudes M_W ~5 similar to those of the 2011 Lorca and the 1919 Jacarilla-Torremendo earthquakes, our synthetic model estimates an occurrence rate of 0.07 events/yr (Table 6), comparable to the rate estimated in the historical catalog, 0.08 ± 0.03 events/yr, from 1800 A.D. Figure 5b shows the contribution of each fault section (black bars) to these total annual earthquake rates calculated from the synthetic catalog. It is important to evaluate the seismic hazard implications of these moderate M_W ~5 earthquakes, due to the severe damage from recent events and the proximity of the faults involved to urban areas with thousands of inhabitants (Figure 1).

5.2. Modeling of Large Magnitude Earthquakes

Paleoseismic information allows us to increase the time window of the actual observations in the EBSZ. Paleoseismic evidence of surface ruptures have been found in the main faults of the system, being dated as post Mid-Pleistocene (Table 2). When referring to surface-rupturing earthquakes, we assume $I_{EMS98} > VII$ and/or $M_W > 6.0$ earthquakes, according to numerous observations that suggest that those magnitudes are more likely to generate surface rupture (e.g., Biasi & Weldon, 2006; McCalpin, 2009).

In Table 5 and Figure 4, we analyze mean RI for large earthquakes obtained by means of paleoseismic research in each fault, except for the PF where there are no simulated $M_W > 6$ events in the PF-2 section to compare with the paleoseismic estimations (Table 2; Roquero et al., 2019). We verify a very good correlation with the recurrence time intervals for simulated events in the AMF and the BSF, and a worse correlation for the CAF and the LTF. For the latter, there is a better fit with the maximum estimations of recurrence than the average. On the contrary, for the CF, the results of recurrence from the simulations imply an important divergence, being much lower than those obtained in paleoseimic sites. At Northern Carboneras fault (CF-2), paleoearthquake evidence (Table 2) suggests an occurrence rate for large earthquakes of around 7.2×10^{-5} events/yr based on trenching results at the El Hacho site for the last 41.5 kyr (Moreno, 2011, see details of the calculation in the Text S1 of Supporting Information). From the reference simulation (catalog 28), the mean annual rate obtained for $M_W > 6$ earthquakes is 9.8×10^{-4} events/yr in CF-2. This means that the rate obtained from the paleoseismic data estimated in the El Hacho site would represent around 7.4% with respect to the result calculated from the synthetic catalog. The degree of fault coupling could be a de-

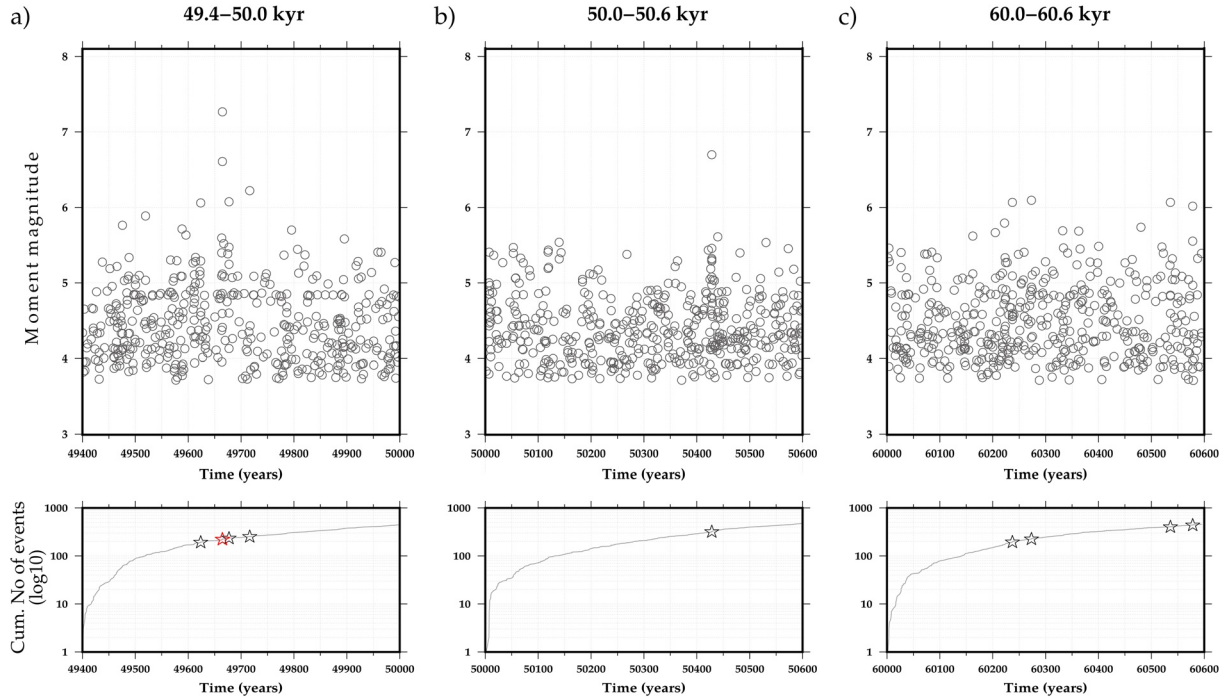

Figure 8. Synthetic seismicity obtained represented in time intervals of 600 years: (a) 49,400-50,000 years; (b) 50,000–50,600 years; and (c) 60,000–60,600 years. Below, cumulative events occurring over the time interval. $M_W > 6$ earthquakes are represented with stars (in red if the magnitude is $M_W > 7$).

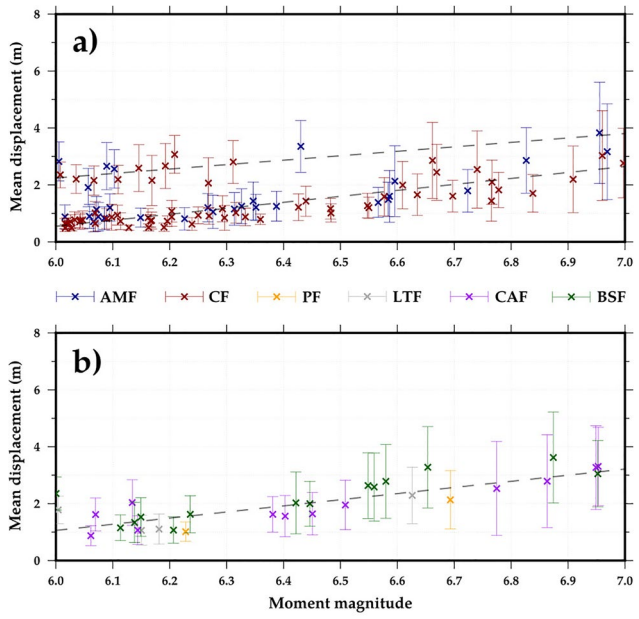

Figure 9. Average displacement in meters over the ruptured fault plane for each $M_W \geq 6.0$ synthetic earthquake, represented with a cross. Vertical bars represent one standard deviation from the mean. Linear trendlines are represented with broken lines. (a) Synthetic events nucleated on the AMF and the CF. (b) Synthetic events nucleated on the PF, the LTF, the CAF, and the BSF.

termining factor of this discrepancy. Our model considers 100% coupling, therefore the data obtained by paleosismology in CF-2 would show much less coupling and could be explained by a certain aseismic behavior in the northern section of this fault (Faulkner et al., 2003). Alternatively, the number of paleoearthquakes observed in trenches of the CF could be a minimum value, possibly meaning lower recurrence periods (Masana et al., 2018).

The earthquake simulator also allows us to obtain the displacement during an event for each element of the model. This enables us to explore the slip distribution during a simulated event along strike and depth. Although analyzing the characteristics of synthetic rupture models is not the aim of this paper, we do assess the mean distances slipped in meters associated with large simulated events. Figure 9 shows the average displacement over the rupture plane for each $M_W \geq 6.0$ synthetic earthquake, represented with a cross. We see that for $6.0 < M_W < 7.0$ events, the mean displacement is typically between the 0.5 and 3.5 m. The displacements obtained for the AMF and the CF (Figure 9a) have a bimodal distribution and reach values above 2 meters in a few $M_W < 6.5$ events. The displacements that we show in Figure 9 are the average values of a slip amplitude that varies along the ruptured fault plane, therefore they could be smaller in the model elements far from the hypocenter and in shallow depths, where we measure the displacement by paleoseismology. In addition to this, we emphasize that the estimations of coseismic displacements obtained in paleoseismic trenches (Table 2) have huge uncertainties, which inhibits their comparison. Even so, we can see that the observations of surface ruptures measured in trenches are generally consistent within an

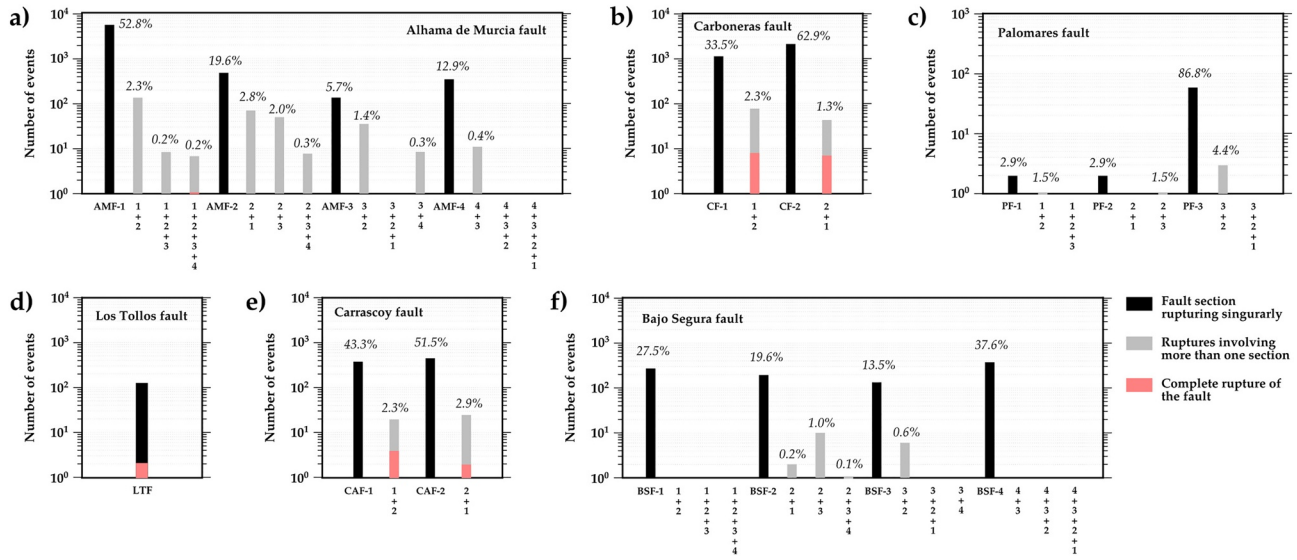

Figure 10. Number of $M_W \geq 5.0$ events associated with ruptures involving various fault sections and the relative percentage to the total number of events generated by that fault. In each rupture propagation scenario, the first section (number) is where the hypocenter of the earthquake is located. (a) Alhama de Murcia Fault catalog; (b) Carboneras Fault catalog; (c) Palomares Fault catalog; (d) Los Tollos Fault catalog; (e) Carrascoy Fault catalog; and (f) Bajo-Segura Fault catalog.

order of magnitude with the values of mean displacements for $M_W < 7.0$ events obtained from our physics-based simulations.

The presence of $M_W > 7.0$ events in our simulated earthquake catalog contrasts with the absence of these large magnitudes in the refined and homogenized historical catalog (Figure 7; IGN-UPM, 2013) and with the lack of evidence of surface paleoruptures with offsets greater than 3 meters among the paleoseismic data (Table 2). This fact may be due to the influence of the time frame in the historical data and the duration variability of the seismic cycles (Figure 8). This problem is especially important in low-strain zones, where seismic catalogs record a minimal fraction of the seismic cycles of the faults. This is in addition to the scarce record of large paleoevents and the limitations of paleoseismology in slow-deformation regions. When we refer to earthquakes associated with metric displacements, with recurrence intervals of thousands of years, the influence of active surface processes on relief is much greater than the influence of tectonic processes. Some evidences observed in paleoseismic sites of the EBSZ cannot be ruled out as being produced by $M_W > 7$ events. For example, Moreno et al. (2016) estimate a magnitude of M_W 7.2 ± 0.3 from the mean slip per event obtained by trenching at CF-1 (considering a complete section rupture), and Martín-Banda (2020) also estimates a maximum M_W 7.1 ± 0.3 considering the joined rupture of the CAF and the LTF by analyzing the age of two events observed in trenches of both faults.

5.3. Fault Segmentation and Extension of the Ruptures

Another objective of our long-term physics-based simulations is to evaluate the influence of fault segmentation in the EBSZ on rupture propagation. We emphasize that the simulator code is not influenced by the subdivision of meshes that represent the fault sections in the model and the ruptures are allowed to propagate from one to another. However, it has been observed that the (re-)nucleation, propagation, and arrest of rupture are very sensitive to complexities in fault geometry (e.g., Douilly et al., 2015; Wollherr et al., 2019). For this reason, what we explore is the influence of changes in geometry (strike and dip), kinematics (rake) and slip rates on the rupture extension. We analyze the following rupture propagation scenarios: (1) if the rupture of a synthetic event is propagated only through the fault section where it is nucleated (single-section rupture); (2) if the rupture is propagated through more than one fault section (multisection rupture); (3) if a fault of the EBSZ can rupture completely (all sections and entire fault plane) in one single event; and (4) if ruptures can jump between faults in a single event (multifault rupture).

Table 7
Multifault Simulated Earthquakes Recorded in the Synthetic Catalog

Faults involved in a multifault rupture[a]	No. of events	Rupture area out of the *nucleating fault* (km^2)	Range of magnitudes M_W	Recurrence interval
CF + PF-1	7	13–64	7.0–7.6	3,065–20,000 years
AMF + LTF	4	37–259	7.0–7.4	6,100–33,700 years
AMF + LTF + PF-3	2	45–103	7.4	12,050 – min. 43,800 years
AMF + PF-3	1	11	7.4	> 100 kyr
PF + LTF	1	9	6.7	> 100 kyr
CAF + LTF	2	17–26	6.9	58,700 years

Fault combinations represent the earthquakes that are nucleated in a fault (in italics) and propagate to another fault in the system. Other possible rupture propagation scenarios that do not appear in the table have also been analyzed, but none of them is recorded during the 100 kyr period simulated in the catalog.
[a]The multifault rupture does not necessarily imply a complete rupture of both faults.

Firstly, we have grouped the simulated catalog events based on the different rupture linkages between sections of the same fault. Figure 10 shows the number of events associated with ruptures involving various fault sections and their relative percentage to the total number of $M_W \geq 5$ events generated by that fault. In each rupture propagation scenario, the first section is where the hypocenter of the earthquake is located. We observe that more than 98% of the events contained in the simulated catalog involve only the fault section where the earthquake is nucleated. However, all seismic sources are capable of propagating the rupture beyond the section where the earthquake is nucleated at some point during a period of 100 kyr. As expected, most synthetic earthquakes involving more than one fault section occur in the sections with the highest estimations of slip rates (AMF-1,2 and CF-1,2) as a greater number of events nucleate in those sections (Figures 10a and 10b).

In the case of the AMF, the CF and the CAF, the synthetic catalog shows some multisection ruptures that involve all fault segments in a single event (Figures 10a, 10b, and 10e). This does not necessarily imply an entire fault length rupture: some of the events extend just beyond the termination of a section and propagate to the adjacent section involved without completely rupturing its entire area. A more detailed analysis of the earthquake rupture surfaces reveals that 22 of these multisection earthquakes (1 in the AMF, 15 in the CF and 6 in the CAF) are certainly the result of rupture of the entire fault length (red bars in Figure 10), with magnitudes ranging between M_W 6.8 and M_W 7.6. The synthetic catalog also records two other complete ruptures (entire fault area) of the LTF (Figure 10d), formed by a single fault section, with a magnitude of M_W 6.6.

In our model the lateral propagation of the BSF is very improbable (Figure 10f), while the rupture of different sections and even different faults (Table 7) on the rest of the system happens several times in our 100 kyr catalog. The main differential characteristic of the BSF is the rake. We have modeled the BSF as reverse faults (Alfaro et al., 2012) while the rest of the faults are oblique and strike-slip faults. To compare the influence of both type of end-member faults we have modeled simple fault ruptures using the Okada (1992) equations (by means of Coulomb 3.4 software; Toda et al. (2005); Lin and Stein (2004)). See the models in Figure S1 of Supporting Information. The reverse fault rupture (Figure S1a) generates small stress transfer lobes on the fault tips, while the strike-slip fault (Figure S1b) generates elongated lobes of stress increment in the strike direction of the fault. If we compare the stress increments on both models (Figure S1c) it is clear that the ability of the reverse faults to propagate laterally is much lower than the ability of the strike-slip ones.

Additionally, the potential multifault rupture in the EBSZ has been evaluated. Table 7 represents the number of simulated earthquakes that propagate into sections belonging to faults different from those where the event is nucleated. We include only the fault combinations corresponding to the earthquakes that are nucleated in a fault and propagate to another fault in the system, thus evaluating the compatibility of their characteristics to favor the slip transfer. During simulations, some of the greatest events that involve com-

plete faults, also generate minor dislocation (isolated patches) of some model cells belonging to nearby faults. We have only considered multifault ruptures those that displace contiguous elements constituting a ≥9 km^2 area in the fault plane to which the rupture is transferred.

Physics-based simulations performed in this research suggest the possibility of large earthquakes capable of propagating through various faults of the system. If a complex multifault rupture occurred at the EBSZ, the earthquake magnitude would be at least M_W 6.7 (Table 7). We observe that the CF would be able to generate a rupture that would extend to the southern section of PF, but without completely rupturing both faults (Table 7). According to the simulations carried out, the CF would generate $M_W > 7.4$ events only when a joined rupture with PF-1 occurred, with a recurrence of up to 20,000 years (Table 7 and Figure 6c).

The AMF is able to transfer slip to model elements in the LTF and the PF (Table 7). We should remember that the RSQSim simulator only generates slip in the elements contained in the modeled sources and no seismic waves are produced, so here can only deduce a re-nucleation by static stress transfer to parallel faults, rather than rupture branching between connected sections (as between CF and PF). Some large earthquakes nucleated in the southern sections of the AMF transfer the slip northeastward along the fault (Figure 10a), and before reaching AMF-4, the rupture "jumps" to the LTF, preferentially. This behavior agrees with the small number of events capable of creating a complete rupture of the AMF (Figure 10a), despite reaching magnitudes up to M_W 7.4 in the resulting synthetic catalog (Figure 6a). It is noteworthy that the combination between the AMF and the LTF is more frequent than between the LTF and laterally contiguous faults, PF, and CAF. It is possible that the LTF, being smaller in size, synchronizes with the other faults more easily than expected. In addition, the short distance (∼6 km) between two large parallel faults such as the AMF and the PF in relation to the fault locking depth (Figure 2) could influence their ability to load simultaneously, the former being much more active than the other. This would favor the slip transfer between the southern sections of the AMF and the LTF versus other nearby fault sections, such as PF-3, whose evidence of Quaternary activity is uncertain (see the reliability ranking in Tables S2 and S3). Furthermore, from a fully-dynamic point of view, we should consider that the jumping rupture between AMF and LTF would depend on the previous stress conditions (Oglesby, 2008). Large stress changes produced by the rupture of adjacent AMF sections, partially influenced by the variation of its orientation with respect to regional stress field (Figure 1), could drive the arrest and renucleation of rupture by dynamic triggering (e.g., Wollherr et al., 2019) at greater distances (to LTF, at least), rather than propagating through connected sections. Also note that the fault geometries can be more complex (secondary branches, stepovers, dip changes at depth) than what we show in the fault model, conditioning the rupture transfer mechanisms (Oglesby, 2008).

Previous studies evaluated the potential for rupture jumping between the faults of the EBSZ through different approaches: by calculating the variation of static stresses (Álvarez-Gómez et al., 2018) and by statistical analysis of potential rupture scenarios based on the slip rates of the faults (Gómez-Novell et al., 2020). Gómez-Novell et al. (2020) suggest probable multifault ruptures between the CF and the PF on the one hand and between the LTF, the CAF, and the BSF on the other, partially thanks to their kinematic compatibility based exclusively on static stress transfer (Álvarez-Gómez et al., 2018). Our results from the physics-based simulations are in agreement with the resulting seismicity obtained by Gómez-Novell et al. (2019), as demonstrated by the similarity between the FMD curves for different sections of the fault system (Figure S2 of Supporting Information). Additionally, our physics-based model allows us to give more insight into the rupture behavior and geometry, allowing to also consider partial ruptures of the fault lengths and the possibility of a transferred rupture between the AMF and the LTF, when these sections were close to its failure limit.

5.4. Advantages and Limitations of Physics-Based Modeling in the EBSZ

Modeling of earthquake processes based on time-dependent nucleation through the physics-based RSQSim simulator, has allowed us to obtain a long synthetic seismic catalog from the EBSZ. As the instrumental and historical earthquake record of the region barely covers a time period of 600 years (from the fifteenth century to the present day), synthetic seismicity permits us to assess more comprehensive magnitude and recurrence statistics. In addition, it allows us to check the available data used in the 3D fault model: fault geometry, deformation rates, kinematics, and frictional properties, evaluating its impact on regional seismicity.

A limitation of our study is the noninclusion of small-size faults and off-fault complexities. For the RSQSim code, simulated seismicity is geographically associated with the 3D faults of the model. By only modeling the larger faults, we have not generated complete low background seismicity in this study. We acknowledge some uncertainty in the results presented here derived from the complexities of the fault zone geometry, especially for the lower magnitudes. For the purposes of this research, we have constructed a simple fault system model, but it is open to future improvements for further analysis, especially regarding the rupture transfer process.

Other limitations to take into account are the uncertainties associated with the input data, an inherent feature of areas with slow-moving faults, such as the EBSZ (Table 3). While some sections of the fault system have been extensively studied, in others, such as PF-3, their knowledge is scarce and their expression raises doubts (see Table S2 in Supporting Information for more detailed data about the accuracy of the parameters). We have run multiple test simulations combining variations of input (frictional and strain) parameters. These demonstrate that, although there are differences between the resulting catalogs, generally there is no significant influence on the magnitude and recurrence statistics. Slip rates are what determine the greatest variations in the models: for example, if the slip rate in PF was higher than estimated so far, a greater synchronization with contiguous faults and, consequently, a higher frequency of connected events would be expected. In this study, we have considered the mean values of the estimations based on the available publications (Tables 3 and S1), but further research on the little-known fault sections of the system (e.g., updated geodetic data) would help to improve the model and the configuration of pre-stress conditions.

As we explained in section 3.3 of Methodology, RSQSim makes a quasi-dynamic approximation to rupture nucleation and propagation. During seismic rupture, no dynamic interactions (i.e., waveforms) and other subsequent dynamic effects (e.g., ground motions and off-fault deformations) are performed. We deal with the quasi-static limitations through the application of some modifications proposed by Richards-Dinger and Dieterich (2012) for the code (see section 3.3) that try to emulate the time-space evolution of the rupture controlled by dynamic interactions. In a fully dynamic context, the pattern of initial stresses, the frictional law and the bulk rheology play a primary role in controlling rupture characteristics (e.g., Douilly et al., 2015; Oglesby, 2008; Wollherr et al., 2019). In relation to the latter, the crustal properties are not fully represented as half elastic space, particularly in continental crust. Viscoelastic relaxation (lower crust - mantle) may influences time-space clustering in a different way that is represented in the model. The results may also be oversimplified as there could be more complex ruptures with fault segments that are further apart than those represented in the current model, and that are not accounted for with a static or quasi-dynamic approach. However, the results that we get with RSQSim are already pointing to insights that are beyond what is observed in the historic record, and helping better understand the incomplete paleoseismic record. So despite the limitations, the method can actually strongly contribute to better understanding seismic hazard in the region.

Numerous probabilistic studies aimed at seismic hazard assessment are based on observed empirical frequencies from seismicity data, often incomplete and insufficient (e.g., McGuire, 2008; Mulargia et al., 2017). The disparity between seismicity behaviors over 100,000 years (Figure 8) and the variability of time between earthquake clusters make us question the completeness methods. Long-term synthetic catalogs based on the simulation of physical processes, in combination with probabilistic methods that incorporate uncertainties into the models, would allow us to improve seismic hazard assessments in the Betic region with a better estimation of worst-case scenarios and recurrence intervals.

6. Conclusions

The application of physics-based earthquake simulations to the Eastern Betic Shear Zone (EBSZ), the main active fault system in the Eastern Betic Cordillera (SE Iberian Peninsula), has allowed the compilation of 100 kyr synthetic seismic catalogs. The RSQSim earthquake simulator code used in this research reproduces the earthquake processes based on the 3D fault geometry, the kinematics, the long-term slip rates and the rate-and-state friction properties. The long-term synthetic seismicity obtained overcome the limitations of the historical earthquake catalog, which is scarce and imprecise compared to the long interseismic periods that characterize the slow-moving faults of the region.

The best-fit simulated catalog obtained in this study statistically matches the observed scaling relations and the mean recurrence time intervals estimated from paleoseismic data. The synthetic catalog shows that the seismogenic sources with the greatest number of nucleated events are the Alhama de Murcia fault (AMF) and the Carboneras fault (CF). This fact is due to > 1 mm/yr slip rates estimated in some of the their sections and possibly because of the predominant strike-slip kinematics that seems to favor the propagation of the rupture.

According to the synthetic model, only about 10% of the simulated events have a magnitude greater than M_W 5.0 but all faults in the fault system are capable of generating $M_W \geq 6.0$ earthquakes over a period of 100,000 years. The synthetic catalogs show various $M_W \geq 7.0$ events in the AMF (max. M_W 7.4) and the CF (max. M_W 7.6), with interevent times of between 5,000 and 40,000 years, and one M_W 7.1 event in the Bajo-Segura fault (BSF). The Carrascoy fault (CAF), located to the NE of the fault system, like the BSF and with a very similar magnitude distribution, records a maximum synthetic earthquake of M_W 6.9. The physics-based simulator reproduces less seismicity in the Palomares fault (PF) and in the Los Tollos fault (LTF), with maximum simulated magnitudes of M_W 6.7 and M_W 6.6, respectively. Although the large $M_W \geq 6$ earthquakes in the EBSZ would have interevent times of a few thousand (in the case of AMF and CF) to tens of thousands of years, the $5 < M_W < 6$ earthquakes, which have been quite destructive recently in this region, could occur over time intervals of less than 1000 years.

The multicycle simulations performed in this study suggest the possibility of large earthquakes capable of propagating through various sections and faults of the system. All seismic sources of the EBSZ are theoretically capable of propagating the rupture beyond the section where the earthquake is nucleated. However, we propose that only the AMF, the CF, the CAF, and the LTF are capable of generating a complete rupture of the fault. The synthetic seismicity model suggests that the most probable generation of large $M_W > 6.7$ earthquakes in the EBSZ would be as a consequence of "jumping" ruptures between nearby faults of the system. The simulated catalog shows joined ruptures (not necessarily implying complete rupture of both faults) between the CF and the southern PF with a recurrence time of less than 20,000 years; and less frequently between the AMF with the LTF and the northern PF by stress transfer. Despite the lower activity, the LTF seems to have a role of linkage between the other faults of the EBSZ, since we observe that it is involved in most of the multifault ruptures.

The great variability of interevent times observed along successive seismic cycles and the strong influence of the time frame support that slow areas that seem to be "muted" during historical times may be just in a period of quiescence but not be inactive. These observations, together with the possibility of complex ruptures jumping between faults, suggest not dismissing the occurrence of larger earthquakes than the low to moderate magnitudes recorded in the scarce earthquake catalog when assessing regional seismic hazard at SE Spain.

Appendix A: RSQSim Simulator Equations

In this study, we have applied the quasi-dynamic earthquake simulator code RSQSim (Dieterich & Richards-Dinger, 2010) to run simulations with the objective of obtaining the synthetic seismicity of the EBSZ. RSQSim is based on a formulation initially developed by Dieterich (1995) with several later enhancements. This project is in current development.

In RSQSim, the frictional shear stress, τ, normal stress, σ, slip speed, V, and state variable, θ, on each model element are related by the following constitutive relation:

$$\tau = \sigma\left[\mu_0 + a\ln\left(\frac{V}{V^*}\right) + b\ln\left(\frac{\theta V^*}{D_C}\right)\right], \tag{A1}$$

where a and b are rate-and-state dimensionless coefficients, V^* is a reference slip speed, D_C is the characteristic distance for slip evolution (10^{-5} m in this study), and μ_0 is the steady-state friction coefficient at the reference slip speed and constant normal stress.

This constitutive relation is combined with the aging form of the state evolution equation that includes the effects of normal stress dependence:

$$\dot{\theta} = 1 - \frac{\theta V}{D_C} - \alpha \frac{\theta \dot{\sigma}}{b\sigma}, \tag{A2}$$

where α is a dimensionless constant (typical laboratory values: 0.25–0.5; in this study, 0.25).

RSQSim also uses 3D elastic dislocation equations (e.g., Okada, 1992) to control stress interactions among fault elements. The shear and normal stress, for each $i - th$ fault element are given by:

$$\dot{\tau}_i = K_{ij}^{\tau} V_j + \dot{\tau}_i^{tect}, \tag{A3}$$

and

$$\dot{\sigma}_i = K_{ij}^{\sigma} V_j + \dot{\sigma}_i^{tect}, \tag{A4}$$

where K_{ij}^{τ} and K_{ij}^{σ} are stiffness matrices derived from elastic interaction solutions; and $\dot{\tau}_i^{tect}$ and $\dot{\sigma}_i^{tect}$ represent tectonic stressing rates.

Data Availability Statement

Data set for this research is available into a data repository (https://doi.org/10.6084/m9.figshare.12909815). GMT package (Wessel et al., 2013) was used to create some figures.

Acknowledgments
This study was supported by the QUAKESTEP project (CGL2017-83931-C3-1-P) funded by the Ministry of Science of Spain. P. Herrero-Barbero thanks the funding support from a Spanish FPU Fellowship and is grateful to GNS Science of New Zealand for providing license and computing facilities during a research visit. C. Williams and P. Villamor were funded by NZ SSIF funds. The authors greatly thank Alice-Agnes Gabriel and Thomas Chartier for comments and suggestions which helped to improve the manuscript. The authors also acknowledge K. Richards-Dinger and R. Benites for their support and helpful discussion on physics-based earthquake simulations.

References

Aki, K., & Richards, P. G. (1980). *Quantitative seismology: Theory and methods*. W. H. Freeman.

Alfaro, P., Bartolomé, R., Borque Arancón, M. J., Estévez, A., García Mayordomo, J., García-Tortosa, F. J., et al. (2012). The Bajo Segura Fault Zone: Active blind thrusting in the Eastern Betic Cordillera (SE Spain).

Alonso-Henar, J., Fernández, C., & Martínez-Díaz, J. J. (2020). Application of the analytic model of general triclinic transpression with oblique extrusion to an active deformation zone: The Alhama de Murcia Fault (SE Iberian Peninsula). *Journal of Structural Geology*, *130*, 103924.

Álvarez-Gómez, J. A., Insua-Arévalo, J. M., Herrero-Barbero, P., Martínez-Díaz, J. J., Canora, C., Alonso-Henar, J., & García Mayordomo, J. (2018). Potencial de encadenamiento de roturas sísmicas en la zona de cizalla de las Béticas Orientales por transferencia de esfuerzos de Coulomb – Seismic ruptures linking potential on the Eastern Betics Shear Zone by Coulomb Stress Transfer. *Avances en el estudio de fallas activas, terremotos y peligrosidad sísmica de Iberia. III Reunión Ibérica sobre Fallas Activas y Paleosismología. Volumen de resúmenes*, 279–282.

Batlló, J., Martínez-Solares, J. M., Macià, R., Stich, D., Morales, J., Garrido, L., et al. (2015). The autumn 1919 Torremendo (Jacarilla) earthquake series (SE Spain).

Biasi, G. P., & Weldon, R. J. (2006). Estimating surface rupture length and magnitude of paleoearthquakes from point measurements of rupture displacement. *Bulletin of the Seismological Society of America*, *96*(5), 1612–1623.

Booth-Rea, G., Azañón, J.-M., Azor, A., & García-Dueñas, V. (2004). Influence of strike-slip fault segmentation on drainage evolution and topography. A case study: the Palomares Fault Zone (southeastern Betics, Spain). *Journal of Structural Geology*, *26*(9), 1615–1632.

Borque, M. J., Sánchez-Alzola, A., Martin-Rojas, I., Alfaro, P., Molina, S., Rosa-Cintas, S., et al. (2019). How much Nubia-Eurasia convergence is accommodated by the NE end of the Eastern Betic Shear Zone (SE Spain)? Constraints from GPS velocities. Journal of Geophysical Research: *Tectonics*, *38*, 1824–1839. https://doi.org/10.1029/2018tc004970

Boschi, E. (2000). Catalog of strong Italian earthquakes from 461 BC to 1997. *Annali di Geofizica*, *43*(4).

Canora, C., Roca, C., Martínez-Díaz, J. J., Insúa-Arévalo, J. M., Martín González, F., Alonso-Henar, J., et al. (2016). Nuevos datos de actividad paleosísmica de la falla de Alhama de Murcia en el abanico de La Salud (segmento Lorca-Totana), Béticas orientales. *Geotemas*, *16*(2), 563–566.

Christophersen, A., Rhoades, D. A., & Colella, H. V. (2017). Precursory seismicity in regions of low strain rate: Insights from a physics-based earthquake simulator. *Geophysical Journal International*, *209*(3), 1513–1525.

Clark, K. J., Nissen, E. K., Howarth, J. D., Hamling, I. J., Mountjoy, J. J., Ries, W. F., et al. (2017). Highly variable coastal deformation in the 2016 MW7.8 Kaikōura earthquake reflects rupture complexity along a transpressional plate boundary. *Earth and Planetary Science Letters*, *474*, 334–344.

Console, R., Carluccio, R., Papadimitriou, E., & Karakostas, V. (2015). Synthetic earthquake catalogs simulating seismic activity in the Corinth Gulf, Greece, fault system. *Journal of Geophysical Research: Solid Earth*, *120*, 326–343. https://doi.org/10.1002/2014JB011765

Console, R., Vannoli, P., & Carluccio, R. (2018). The seismicity of the Central Apennines (Italy) studied by means of a physics-based earthquake simulator. *Geophysical Journal International*, *212*(2), 916–929.

De Larouzière, F., Bolze, J., Bordet, P., Hernandez, J., Montenat, C., & d'Estevou, P. O. (1988). The Betic segment of the lithospheric Trans-Alboran shear zone during the Late Miocene. *Tectonophysics*, *152*(1–2), 41–52.

Dieterich, J. H. (1978). Time-dependent friction and the mechanics of stick-slip. In *Rock friction and earthquake prediction* (pp. 790–806). Springer.
Dieterich, J. H. (1979). Modeling of rock friction: 1. Experimental results and constitutive equations. *Journal of Geophysical Research*, *84*(B5), 2161–2168.
Dieterich, J. H. (1995). Earthquake simulations with time-dependent nucleation and long-range interactions.
Dieterich, J. H., & Richards-Dinger, K. B. (2010). Earthquake recurrence in simulated fault systems. *Pure and Applied Geophysics*, *8*(167), 1087–1104.
Douilly, R., Aochi, H., Calais, E., & Freed, A. M. (2015). Three-dimensional dynamic rupture simulations across interacting faults: The M w 7.0, 2010, Haiti earthquake. *Journal of Geophysical Researc: Solid Earth*, *120*, 1108–1128.
Echeverria, A., Khazaradze, G., Asensio, E., Gárate, J., Dávila, J. M., & Suriñach, E. (2013). Crustal deformation in eastern Betics from CuaTeNeo GPS network. *Tectonophysics*, *608*, 600–612.
Echeverria, A., Khazaradze, G., Asensio, E., & Masana, E. (2015). Geodetic evidence for continuing tectonic activity of the Carboneras fault (SE Spain). *Tectonophysics*, *663*, 302–309.
Estay, N. P., Yáñez, G., Carretier, S., Lira, E., & Maringue, J. (2016). Seismic hazard in low slip rate crustal faults, estimating the characteristic event and the most hazardous zone: study case San Ramón Fault, in southern Andes. *Natural Hazards and Earth System Sciences*, *16*(12).
Faulkner, D., Lewis, A., & Rutter, E. (2003). On the internal structure and mechanics of large strike-slip fault zones: field observations of the carboneras fault in southeastern spain. *Tectonophysics*, *367*(3–4), 235–251.
Ferrater, M., Ortuño, M., Masana, E., Martínez-Díaz, J. J., Pallàs, R., Perea, H., et al. (2017). Lateral slip rate of Alhama de Murcia fault (SE Iberian Peninsula) based on a morphotectonic analysis: Comparison with paleoseismological data. *Quaternary International*, *451*, 87–100.
Ferrater, M., Ortuño, M., Masana, E., Pallàs, R., Perea, H., Baize, S., et al. (2016). Refining seismic parameters in low seismicity areas by 3D trenching: The Alhama de Murcia fault, SE Iberia. *Tectonophysics*, *680*, 122–128.
Ferrater, M., Silva, P. G., Ortuño, M., Rodríguez-Pascua, M. Á., & Masana, E. (2015). Archaeoseismological analysis of a Late Bronze Age site on the Alhama de Murcia fault, SE Spain. *Geoarchaeology*, *30*(2), 151–164.
Field, E., Dawson, T., Felzer, K., Frankel, A., Gupta, V., Jordan, T., et al. (2008). The uniform California earthquake rupture forecast, Version 2 (UCERF 2) USGS. Open-File Report 2007-1437 (p. 203). CGS Special Report.
Gamage, P., & Venkatesan, S. (2019). Evaluation of seismic hazard in low to moderate seismic regions, Sri Lanka-a case study. *Journal of Seismology*, *23*(3), 579–611.
García-Mayordomo, J. (2005). *Caracterización y Análisis de la Peligrosidad Sísmica en el Sureste de España*. Doctoral dissertation. Universidad Complutense de Madrid.
García-Mayordomo, J., Gaspar-Escribano, J. M., & Benito, B. (2007). Seismic hazard assessment of the Province of Murcia (SE Spain): analysis of source contribution to hazard. *Journal of Seismology*, *11*(4), 453–471.
García-Mayordomo, J., Insua-Arévalo, J. M., Martínez-Díaz, J. J., Jiménez-Díaz, A., Martín-Banda, R., Martín Alfageme, S. R., et al. (2012). The Quaternary active faults database of Iberia (QAFI v. 2.0).
García-Mayordomo, J., Martín-Banda, R., Insua-Arévalo, J. M., Álvarez-Gómez, J. A., Martínez-Díaz, J. J., & Cabral, J. (2017). Active fault databases: building a bridge between earthquake geologists and seismic hazard practitioners, the case of the QAFI v.3 database. *Natural Hazards and Earth System Sciences*, *17*(8), 1447.
García-Mayordomo, J., & Martínez-Díaz, J. (2006). Caracterización sísmica del anticlinorio del Bajo Segura (Alicante): Fallas del Bajo Segura, Torrevieja y San Miguel de Salinas. *Geogaceta*, *40*, 19–22.
Gaspar-Escribano, J. M., Rivas-Medina, A., Parra, H., Cabañas, L., Benito, B., Ruiz Barajas, S., & Martínez Solares, J. M. (2015). Uncertainty assessment for the seismic hazard map of Spain. *Engineering Geology*, *199*, 62–73.
Gilchrist, J. J. (2015). *Applications of multi-cycle earthquake simulations to earthquake hazard*. Doctoral dissertation. UC Riverside.
Gimbutas, Z., Greengard, L., Barall, M., & Tullis, T. E. (2012). On the calculation of displacement, stress, and strain induced by triangular dislocations. *Bulletin of the Seismological Society of America*, *102*(6), 2776–2780.
Giner, J. J., Molina, S., & Jáuregui, P. J. (2003). Sismicidad en la Comunidad Valenciana (CV). *Física de la Tierra*, *15*, 163–187.
Gómez-Novell, O., Chartier, T., García-Mayordomo, J., Ortuño, M., Masana, E., Insua-Arévalo, J. M., & Scotti, O. (2019). *Modeling earthquake multi-fault ruptures across complex fault systems for probabilistic seismic hazard assessment: The Eastern Betics shear zone*. [WWW Document]. Retrieved from https://doi.org/10.17632/pt32rrncdm.1
Gómez-Novell, O., Chartier, T., García-Mayordomo, J., Ortuño, M., Masana, E., Insua-Arévalo, J. M., & Scotti, O. (2020). Modeling earthquake rupture rates in fault systems for seismic hazard assessment: The Eastern Betics Shear Zone. *Engineering Geology*, *265*, 105452.
Gràcia, E., Bartolomé, R., Lo Iacono, C., Moreno, X., Stich, D., Martínez-Diaz, J. J., et al. (2012). Acoustic and seismic imaging of the Adra Fault (NE Alboran Sea): in search of the source of the 1910 Adra earthquake. *Natural Hazards and Earth System Sciences*, *12*(11), 3255–3267.
Hayes, G. P., Briggs, R. W., Sladen, A., Fielding, E. J., Prentice, C., Hudnut, K., et al. (2010). Complex rupture during the 12 January 2010 Haiti earthquake. *Nature Geoscience*, *3*(11), 800–805.
Herrero-Barbero, P., Álvarez-Gómez, J. A., Martínez-Díaz, J. J., & Klimowitz, J. (2020). Neogene basin inversion and recent slip rate distribution of the northern termination of the Alhama de Murcia Fault (Eastern Betic Shear Zone, SE Spain). Journal of Geophysical Research: *Tectonics*, *39*(7), e2019TC005750. https://doi.org/10.1029/2019TC005750
Herrero-Barbero, P., Álvarez-Gómez, J. A., Williams, C., Villamor, P., Insua-Arévalo, J. M., Alonso-Henar, J., & Martínez-Díaz, J. J. (2021). *Dataset - physics-based earthquake simulations in slow-moving faults: A case study from the Eastern betic shear zone (SE Spain)*. Retrieved from https://doi.org/10.6084/m9.figshare.12909815
IGN. (2019). *The Spanish seismic catalog. Catálogo Sísmico Nacional*. IGN – Instituto Geográfico Nacional. Retrieved from https://www.ign.es/web/ign/portal/sis-catalogo-terremotos
IGN-UPM. (2013). Actualización de mapas de peligrosidad sísmica de España 2012. (Vol. 267). Centro Nacional de Información Geográfica.
Insua-Arévalo, M., García-Mayordomo, J., Salazar, Á., Rodríguez-Escudero, E., Martín-Banda, R., Álvarez-Gómez, J. A., et al. (2015). Paleoseismological evidence of Holocene activity of the Los Tollos Fault (Murcia, SE Spain): a lately formed Quaternary tectonic feature of the Eastern Betic Shear Zone.
Ishibashi, K. (2004). Status of historical seismology in Japan. *Annals of Geophysics*, *47*(2–3).
Kearse, J., Kaneko, Y., Little, T., & Van Dissen, R. (2019). Curved slickenlines preserve direction of rupture propagation. *Geology*, *47*(9), 838–842.

Koulali, A., Ouazar, D., Tahayt, A., King, R., Vernant, P., Reilinger, R., et al. (2011). New GPS constraints on active deformation along the Africa–Iberia plate boundary. *Earth and Planetary Science Letters*, *308*(1–2), 211–217.
Lapusta, N., & Liu, Y. (2009). Three-dimensional boundary integral modeling of spontaneous earthquake sequences and aseismic slip. *Journal of Geophysical Research*, *114*, B09303. https://doi.org/10.1029/2008jb005934
Leonard, M. (2010). Earthquake fault scaling: Self-consistent relating of rupture length, width, average displacement, and moment release. *Bulletin of the Seismological Society of America*, *100*(5A), 1971–1988. https://doi.org/10.1785/0120090189
Lin, J., & Stein, R. S. (2004). Stress triggering in thrust and subduction earthquakes and stress interaction between the southern San Andreas and nearby thrust and strike-slip faults. *Journal of Geophysical Research*, *109*, B02303. https://doi.org/10.1029/2003jb002607
Litchfield, N. J., Wyss, B., Christophersen, A., Thomas, R., Berryman, K., Henshaw, P., & Villamor, P. (2013). *Guidelines for compilation of neotectonic faults, Folds and fault sources: GEM faulted Earth*. Institute of Geological and Nuclear Sciences Limited.
Liu, M., Stein, S., & Wang, H. (2011). 2000 years of migrating earthquakes in North China: How earthquakes in midcontinents differ from those at plate boundaries. *Lithosphere*, *3*(2), 128–132.
López-Comino, J. A., Mancilla, F. d. L., Morales, J., & Stich, D. (2012). Rupture directivity of the 2011, Mw 5.2 Lorca earthquake (Spain). *Geophysical Research Letters*, *39*, L03301. https://doi.org/10.1029/2011gl050498
Martí, A., Queralt, P., Marcuello, A., Ledo, J., Rodríguez-Escudero, E., Martínez-Díaz, J. J., et al. (2020). Magnetotelluric characterization of the Alhama de Murcia Fault (Eastern Betics, Spain) and study of magnetotelluric interstation impedance inversion. *Earth Planets and Space*, *72*(1), 16.
Martín-Banda, R. (2020). *Segmentación y evolución reciente del Sistema de Fallas de la Sierra de Carrascoy: Implicaciones en su potencial sismogénico*. Doctoral dissertation. Universidad Complutense.
Martín-Banda, R., García-Mayordomo, J., Insua-Arévalo, J. M., Salazar, Á. E., Rodríguez-Escudero, E., Álvarez-Gómez, J. A., et al. (2016). New insights on the seismogenic potential of the Eastern Betic Shear Zone (SE Iberia): Quaternary activity and paleoseismicity of the SW segment of the Carrascoy Fault Zone. Journal of Geophysical Research: *Tectonics*, *35*, 55–75. https://doi.org/10.1002/2015tc003997
Martínez-Díaz, J. J. (1998). *Neotectonica y Tectonica Activa del oeste de Murcia y sur de Almeria (Cordillera Betica)*. Doctoral dissertation. Universidad Complutense de Madrid.
Martínez-Díaz, J. J., Alonso-Henar, J., Insua-Arévalo, J. M., Canora, C., García-Mayordomo, J., Rodríguez-Escudero, E., et al. (2018). Geological evidences of surface rupture related to a seventeenth century destructive earthquake in Betic Cordillera (SE Spain): constraining the seismic hazard of the Alhama de Murcia fault. *Journal of Iberian Geology*, *45*(1), 73–86.
Martínez-Díaz, J. J., Bejar-Pizarro, M., Álvarez-Gómez, J. A., Mancilla, F. d. L., Stich, D., Herrera, G., & Morales, J. (2012). Tectonic and seismic implications of an intersegment rupture. *Tectonophysics*, *546–547*, 28–37.
Martínez-Díaz, J. J., Masana, E., & Ortuño, M. (2012). Active tectonics of the Alhama de Murcia fault, Betic Cordillera, Spain. *Journal of Iberian Geology*, *38*(1), 253–270.
Martınez-Solares, J., & Mezcua, J. (2002). Catálogo sısmico de la Penınsula Ibérica (880 aC-1900). (Vol. 18, p. 444). Instituto Geográfico Nacional–Monografia.
Masana, E., Martínez-Díaz, J. J., Hernández-Enrile, J., & Santanach, P. (2004). The Alhama de Murcia fault (SE Spain), a seismogenic fault in a diffuse plate boundary: Seismotectonic implications for the Ibero-Magrebian region. *Journal of Geophysical Research*, *109*, B01301. https://doi.org/10.1029/2002jb002359
Masana, E., Moreno, X., Gràcia, E., Pallàs, R., Ortuño, M., López, R., et al. (2018). First evidence of paleoearthquakes along the Carboneras Fault Zone (SE Iberian Peninsula): Los Trances site. *Geológica Acta*, *16*(4), 461–476.
McCalpin, J. P. (2009). *Paleoseismology*. Academic press.
McGuire, R. K. (2008). Probabilistic seismic hazard analysis: Early history. *Earthquake Engineering and Structural Dynamics*, *37*(3), 329–338.
Moreno, X. (2011). *Neotectonic and paleoseismic onshore-offshore integrated study of the Carboneras fault (Eastern Betics, SE Iberia)/Estudio integrado tierra-mar de la Neotectonica y Paleosismología de la Falla de Carboneras (Béticas Orientales, SE Península Ibérica)*. Doctoral dissertation. Universitat de Barcelona.
Moreno, X., Gràcia, E., Bartolomé, R., Martínez-Loriente, S., Perea, H., de la Peña, L. G., et al. (2016). Seismostratigraphy and tectonic architecture of the Carboneras Fault offshore based on multiscale seismic imaging: Implications for the Neogene evolution of the NE Alboran Sea. *Tectonophysics*, *689*, 115–132.
Moreno, X., Masana, E., Pallàs, R., Gràcia, E., Rodés, Á., & Bordonau, J. (2015). Quaternary tectonic activity of the Carboneras Fault in the La Serrata range (SE Iberia): Geomorphological and chronological constraints. *Tectonophysics*, *663*, 78–94.
Mulargia, F., Stark, P. B., & Geller, R. J. (2017). Why is probabilistic seismic hazard analysis (PSHA) still used? *Physics of the Earth and Planetary Interiors*, *264*, 63–75.
Murphy, P. (2019). *Los terremotos de Almería de 1804. En el archivo histórico nacional*. Instituto Geográfico Nacional (IGN).
Niemeijer, A. R., & Vissers, R. L. M. (2014). Earthquake rupture propagation inferred from the spatial distribution of fault rock frictional properties. *Earth and Planetary Science Letters*, *396*, 154–164. https://doi.org/10.1016/j.epsl.2014.04.010
Nocquet, J.-M. (2012). Present-day kinematics of the Mediterranean: A comprehensive overview of GPS results. *Tectonophysics*, *579*, 220–242.
Nur, A., & Cline, E. H. (2000). Poseidon's horses: Plate tectonics and earthquake storms in the Late Bronze Age Aegean and Eastern Mediterranean. *Journal of Archaeological Science*, *27*(1), 43–63.
Oglesby, D. (2008). Rupture termination and jump on parallel offset faults. *Bulletin of the Seismological Society of America*, *98*(1), 440–447.
Okada, Y. (1992). Internal deformation due to shear and tensile faults in a half-space. *Bulletin of the Seismological Society of America*, *82*(2), 1018–1040.
Ortuño, M., Masana, E., García-Meléndez, E., Martínez-Díaz, J., Štěpančíková, P., Cunha, P. P., et al. (2012). An exceptionally long paleoseismic record of a slow-moving fault: The Alhama de Murcia fault (Eastern Betic shear zone, Spain). *Bulletin*, *124*(9–10), 1474–1494.
Oskin, M. E., Arrowsmith, J. R., Corona, A. H., Elliott, A. J., Fletcher, J. M., Fielding, E. J., et al. (2012). Near-field deformation from the El Mayor-Cucapah earthquake revealed by differential LIDAR. *Science*, *335*(6069), 702–705.
Page, M. T., & Hough, S. E. (2014). The new madrid seismic zone: Not dead yet. *Science*, *343*(6172), 762–764.
Perea, H., & Atakan, K. (2007). Influence of slow active faults in probabilistic seismic hazard assessment: the northwestern margin of the València trough. *Natural Hazards*, *43*(3), 379–396.
Perea, H., Gràcia, E., Alfaro, P., Bartolomé, R., Lo Iacono, C., Moreno, X., & Masana, E. (2012). Quaternary active tectonic structures in the offshore Bajo Segura basin (SE Iberian Peninsula - Mediterranean Sea). *Natural Hazards and Earth System Sciences*, *12*(10), 3151–3168.
Reasenberg, P. (1985). Second-order moment of central California seismicity, 1969-1982. *Journal of Geophysical Research*, *90*(B7), 5479–5495.

Reicherter, K., & Hübscher, C. (2007). Evidence for a seafloor rupture of the Carboneras Fault Zone (southern Spain): Relation to the 1522 Almería earthquake? *Journal of Seismology*, *11*(1), 15–26.

Richards-Dinger, K., & Dieterich, J. H. (2012). RSQSim earthquake simulator. *Seismological Research Letters*, *83*(6), 983–990. https://doi.org/10.1785/0220120105

Rivas-Medina, A., Benito, B., & Gaspar-Escribano, J. M. (2018). Approach for combining fault and area sources in seismic hazard assessment: Application in south-eastern Spain. *Natural Hazards and Earth System Sciences*, *18*(11), 2809–2823.

Robinson, R., Van Dissen, R., & Litchfield, N. (2011). Using synthetic seismicity to evaluate seismic hazard in the Wellington region, New Zealand. *Geophysical Journal International*, *187*(1), 510–528. https://doi.org/10.1111/j.1365-246X.2011.05161.x

Rodríguez-Escudero, E. (2017). *Implicaciones de la Estructura Interna de una Zona de Falla Activa en la Génesis de Terremotos*. Doctoral dissertation. Universidad Autónoma de Madrid.

Rodríguez-Escudero, E., Martínez-Díaz, J., Álvarez-Gómez, J., Insua-Arévalo, J., & Capote del Villar, R. (2014). Tectonic setting of the recent damaging seismic series in the Southeastern Betic Cordillera, Spain. *Bulletin of Earthquake Engineering*, *12*(5).

Roquero, E., Silva, P. G., Rodríguez-Pascua, M. A., Bardají, T., Elez, J., Carrasco-García, P., & Giner-Robles, J. L. (2019). Analysis of faulted fan surfaces and paleosols in the Palomares Fault Zone (Betic Cordillera, SE Spain): Paleoclimatic and paleoseismic implications. *Geomorphology*, *342*, 88–102.

Rundle, J. B. (1988). A physical model for earthquakes: 2. Application to southern California. *Journal of Geophysical Research*, *93*(B6), 6255–6274.

Sachs, M. K., Heien, E. M., Turcotte, D. L., Yikilmaz, M. B., Rundle, J. B., & Kellogg, L. H. (2012). Virtual California earthquake simulator. *Seismological Research Letters*, *83*(6), 973–978.

Sanz de Galdeano, C. (1990). Geologic evolution of the Betic Cordilleras in the Western Mediterranean, Miocene to the present. *Tectonophysics*, *172*(1–2), 107–119.

Sanz de Galdeano, C., López Garrido, Á. C., García Tortosa, F. J., et al. (1998). Nuevos datos para la estimación de los valores de levantamiento desde el Tortoniense Superior a la actualidad en la parte centro-occidental de la Sierra de Carrascoy (provincia de Murcia).

Savage, J. C. (1983). A dislocation model of strain accumulation and release at a subduction zone. *Journal of Geophysical Research*, *88*(B6), 4984–4996.

Scholz, C. H. (1998). Earthquakes and friction laws. *Nature*, *391*(6662), 37–42.

Serpelloni, E., Vannucci, G., Pondrelli, S., Argnani, A., Casula, G., Anzidei, M., et al. (2007). Kinematics of the Western Africa-Eurasia plate boundary from focal mechanisms and GPS data. *Geophysical Journal International*, *169*(3), 1180–1200.

Shaw, B. E., Milner, K. R., Field, E. H., Richards-Dinger, K., Gilchrist, J. J., Dieterich, J. H., & Jordan, T. H. (2018). A physics-based earthquake simulator replicates seismic hazard statistics across California. *Science Advances*, *4*(8), eaau0688. https://doi.org/10.1126/sciadv.aau0688

Silva, P. G. (1994). *Evolución geodinámica de la depresión del Guadalentín (Murcia) desde el mioceno superior hasta la actualidad: Neotectónica y geomorfología*. Doctoral dissertation. Universidad Complutense de Madrid.

Silva, P. G., Goy, J., Zazo, C., & Bardaji, T. (2003). Fault-generated mountain fronts in southeast Spain: geomorphologic assessment of tectonic and seismic activity. *Geomorphology*, *50*(1–3), 203–225.

Steacy, S. J., & McCloskey, J. (1999). Heterogeneity and the earthquake magnitude-frequency distribution. *Geophysical Research Letters*, *26*(7), 899–902.

Stich, D., Batlló, J., Morales, J., Macià, R., & Dineva, S. (2003). Source parameters of the MW= 6.1 1910 Adra earthquake (southern Spain). *Geophysical Journal International*, *155*(2), 539–546.

Stich, D., Martínez-Solares, J. M., Custódio, S., Batlló, J., Martín, R., Teves-Costa, P., & Morales, J. (2020). Seismicity of the Iberian Peninsula. In *The Geology of Iberia: A Geodynamic approach* (pp. 11–32). Springer.

Stirling, M. W., Wesnousky, S. G., & Shimazaki, K. (1996). Fault trace complexity, cumulative slip, and the shape of the magnitude-frequency distribution for strike-slip faults: A global survey. *Geophysical Journal International*, *124*(3), 833–868.

Taboada, A., Bousquet, J., & Philip, H. (1993). Coseismic elastic models of folds above blind thrusts in the Betic Cordilleras (Spain) and evaluation of seismic hazard. *Tectonophysics*, *220*(1–4), 223–241.

Toda, S., Stein, R. S., Richards-Dinger, K., & Bozkurt, S. B. (2005). Forecasting the evolution of seismicity in southern California: Animations built on earthquake stress transfer. *Journal of Geophysical Research*, *110*(B5). https://doi.org/10.1029/2004jb003415

Villamor, P. (2002). *Cinemática Terciaria y Cuaternaria de la Falla de Alentejo-Plasencia y su influencia en la peligrosidad sísmica de la Península Ibérica* (p. 343). Doctoral dissertation. Universidad Complutense Madrid.

Wells, D. L., & Coppersmith, K. J. (1994). New empirical relationships among magnitude, rupture length, rupture width, rupture area, and surface displacement. *Bulletin of the Seismological Society of America*, *84*(4), 974–1002.

Wessel, P., Smith, W. H. F., Scharroo, R., Luis, J., & Wobbe, F. (2013). Generic mapping tools: Improved version released. *Eos Trans. AGU*, *94*(45), 409–410.

Wiemer, S. (2001). A software package to analyze seismicity: ZMAP. *Seismological Research Letters*, *72*(3), 373–382.

Wilson, J. M., Yoder, M. R., Rundle, J. B., Turcotte, D. L., & Schultz, K. W. (2018). Earthquakes and Multi-Hazards Around the Pacific Rim. *Spatial evaluation and verification of earthquake simulators* (Vol. I, pp. 85–99). Springer.

Wollherr, S., Gabriel, A. A., & Mai, P. M. (2019). Landers 1992 "reloaded": Integrative dynamic earthquake rupture modeling. *Journal of Geophysical Research: Solid Earth*, *124*, 6666–6702. https://doi.org/10.1029/2018jb016355